

IDENTIFYING 3D GENOME ORGANIZATION IN DIPLOID ORGANISMS VIA EUCLIDEAN DISTANCE GEOMETRY*

ANASTASIYA BELYAEVA[†], KAIE KUBJAS[‡], LAWRENCE J. SUN[†], AND CAROLINE UHLER[†]

Abstract. The spatial organization of the DNA in the cell nucleus plays an important role for gene regulation, DNA replication, and genomic integrity. Through the development of chromosome conformation capture experiments (such as 3C, 4C, Hi-C) it is now possible to obtain the contact frequencies of the DNA at the whole-genome level. In this paper, we study the problem of reconstructing the 3D organization of the genome from such whole-genome contact frequencies. A standard approach is to transform the contact frequencies into noisy distance measurements and then apply semidefinite programming (SDP) formulations to obtain the 3D configuration. However, neglected in such reconstructions is the fact that most eukaryotes including humans are diploid and therefore contain two copies of each genomic locus. We prove that the 3D organization of the DNA is not identifiable from distance measurements derived from contact frequencies in diploid organisms. In fact, there are infinitely many solutions even in the noise-free setting. We then discuss various additional biologically relevant and experimentally measurable constraints (including distances between neighboring genomic loci and higher-order interactions) and prove identifiability under these conditions. Furthermore, we provide SDP formulations for computing the 3D embedding of the DNA with these additional constraints and show that we can recover the true 3D embedding with high accuracy from both noiseless and noisy measurements. Finally, we apply our algorithm to real pairwise and higher-order contact frequency data and show that we can recover known genome organization patterns.

Key words. 3D genome organization; Hi-C; diploid organisms; Euclidean distance geometry; semidefinite programming, systems of polynomial equations.

AMS subject classifications. 51K05, 92E10, 90C22, 52C25, 14P05.

1. Introduction. It is now well established that the spatial organization of the genome in the cell nucleus plays an important role for cellular processes including gene regulation, DNA replication, and the maintenance of genomic integrity [11, 39, 40]. Notably, a recent study [43] showed a causal link between three-dimensional (3D) genome organization and gene regulation, where gene repositioning was induced and subsequent changes in gene expression were observed. This motivates the development of methods to reconstruct the 3D structure of the genome to study its functions.

The genetic information in cells is contained in the DNA, which is organized into chromosomes and packed into the cell nucleus. Chromosome conformation capture techniques (such as 3C, 4C, Hi-C, Capture-C) have enabled the interrogation of the contact frequencies between pairs of genomic loci at the whole-genome scale [12, 37, 24, 20]. In Hi-C, for example, interacting chromosome regions are crosslinked (i.e., frozen),

*Submitted.

Funding: Anastasiya Belyaeva was supported by an NSF Graduate Research Fellowship (1122374), the Abdul Latif Jameel World Water and Food Security Lab (J-WAFS) at MIT and the MIT J-Clinic for Machine Learning and Health. Kaie Kubjas was supported by the European Union’s Horizon 2020 research and innovation programme: Marie Skłodowska-Curie grant agreement No. 748354, research carried out at LIDS, MIT and Team PolSys, LIP6, Sorbonne University. Caroline Uhler was partially supported by NSF (DMS-1651995), ONR (N00014-17-1-2147 and N00014-18-1-2765), IBM, and a Simons Investigator Award.

[†]Laboratory for Information and Decision Systems, Department of Electrical Engineering and Computer Science, and Institute for Data, Systems and Society, Massachusetts Institute of Technology, Cambridge, MA (belyaeva@mit.edu, sunl@mit.edu, cuhler@mit.edu).

[‡]Department of Mathematics and Systems Analysis, Aalto University, Espoo, Finland (kaie.kubjas@aalto.fi).

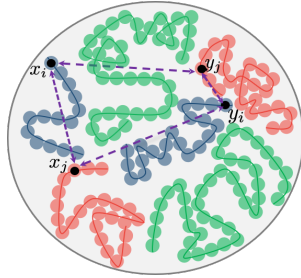


FIG. 1. Schematic of the diploid genome. Nucleus with green, blue and red curves depicting three homologous pairs of chromosomes. In the unphased setting, the measured distance between loci i and j corresponds to the sum of the four distances (denoted in purple) between two pairs of homologous loci x_i, y_i and x_j, y_j .

the DNA is then fragmented, the crosslinked fragments are ligated, and paired-end sequencing is applied to the ligation products and mapped to a reference genome [24]. By binning the genome and ascribing each read pair into the corresponding bin, one obtains a contact frequency matrix between genomic loci that is commonly of the size $10^6 \times 10^6$.

Different computational approaches for reconstructing the 3D genome organization from contact frequency data have been considered. Distance-based approaches convert contact frequencies F_{ij} into spatial distances D_{ij} and find a Euclidean embedding of the points in 3D [14, 46, 23, 35]. Ensemble methods such as MCMC5C and BACH [36, 19] learn a set of possible 3D structures by defining a probabilistic model for contact frequencies and generating an ensemble of structures via MCMC sampling. Other ensemble methods include molecular dynamics simulations that model DNA as a polymer and output an ensemble of 3D structures [25, 27, 13, 32]. Finally, statistical methods have also been proposed that directly model contact counts instead of distances, using for example the Poisson distribution [42], and maximize the log-likelihood of the data to infer the 3D genome organization.

Almost all existing methods make the simplifying assumption that the genome is haploid, when in fact most organisms of interest including humans are diploid, i.e. there are two copies of each chromosome known as *homologous chromosomes*. For example, human cells contain two copies of 23 chromosomes each. The challenge is that the contact frequency data from chromosome conformation capture experiments is generally *unphased*, meaning that the copies of each chromosome cannot be distinguished. As a result, if the DNA is modeled as a string of beads containing two copies of each bead i for $1 \leq i \leq n$, then the measured contact frequencies result in an $n \times n$ matrix, from which we would like to infer the 3D embedding of $2n$ points. This problem cannot be solved by classical methods for 3D genome reconstruction methods such as those mentioned above. With significant experimental efforts, phased data can be obtained [7, 8] and used in order to reconstruct the 3D genome organization [4]. However, such data is rare and costly.

In this paper, we provide a computational method for inferring the 3D diploid organization of the genome without relying on phased data. In particular, we consider a distance-based approach and use Euclidean distance geometry to obtain the 3D diploid structure of the genome. The precise mathematical problem considered in this paper is as follows and illustrated in Figure 1. DNA is modeled as a string of beads, that contains two copies of each bead i for $1 \leq i \leq n$. We would like to infer the

location of the two copies of each bead, which we denote by $x_i \in \mathbb{R}^3$ and $y_i \in \mathbb{R}^3$. Since for unphased data, the two copies of each bead cannot be distinguished, the problem is to identify the 3D configuration ($2n \times 3$ matrix), i.e. $x_1, \dots, x_n, y_1, \dots, y_n \in \mathbb{R}^3$ (up to translation and rotation), from the composite distance measurements D_{ij} , $1 \leq i \neq j \leq n$ ($n \times n$ matrix), corresponding to the sum of the distances between either copy of bead i and j , i.e.,

$$D_{ij} = \|x_i - x_j\|^2 + \|x_i - y_j\|^2 + \|y_i - x_j\|^2 + \|y_i - y_j\|^2.$$

In the haploid or phased setting, this problem boils down to the standard Euclidean distance geometry problem. This problem has a long history: in the classical setting with no missing values, this problem can be solved via the classical multidimensional scaling (cMDS) algorithm that is based on spectral decomposition followed by dimensionality reduction; see [9] for an overview. Other approaches for the Euclidean embedding and completion problems, including in the presence of missing values, are non-convex formulations [15, 28] as well as semidefinite relaxations [1, 16, 5, 26, 44, 45].

A naive approach in the unphased diploid setting is to assume that the four distances that make up our measured composite distance D_{ij} are equal and solve the corresponding Euclidean embedding problem. However, it is evident from single-cell imaging studies that the four distances in D_{ij} can be wildly different [3, 30]. Hence this approach cannot provide realistic embeddings. While, a simple dimension argument ($6n$ variables versus $\binom{n}{2}$ constraints) suggests that the 3D genome configuration is uniquely identifiable, one of the main results of our paper is that the 3D diploid genome configuration is not identifiable from unphased data. In fact, we show that there are infinitely many configurations that satisfy the constraints imposed by D_{ij} , even in the noiseless setting (section 2, Theorem 2.1).

We therefore consider additional biologically relevant and experimentally measurable constraints and study identifiability of the 3D diploid structure under these constraints. First, we take into account distances between neighboring beads, i.e. $\|x_i - x_{i+1}\|^2$ and $\|y_i - y_{i+1}\|^2$ on each chromosome. While we show that this yields unique identifiability for configurations in 2D, there are still infinitely many configurations in 3D, which is of primary interest for genome modeling (section 3, Proposition 3.1, Proposition 3.2). To obtain identifiability in 3D, we consider adding constraints based on contact frequencies between three or more loci simultaneously. The measurement of such higher-order contact frequencies has recently been enabled by experimental assays such as SPRITE [33], C-walks [31] and GAM [2]. We prove that this information can be used to uniquely identify the 3D genome organization from unphased data in the noiseless setting (section 4, Theorem 4.1).

Finally, we provide an SDP formulation for obtaining the 3D diploid configuration from noisy measurements (section 5) and show based on simulated data that our algorithm has good performance and that it is able to recover known genome organization patterns when applied to real contact frequency data collected from human lymphoblastoid cells (section 6).

2. Unidentifiability from pairwise distance constraints. In the remainder of the paper we denote the true but unknown coordinates of the homologous loci by x_i^* and y_i^* and the corresponding noiseless distances by D_{ij}^* while the symbols x_i and y_i denote the variables that we want to solve for. While from a biological perspective the relevant setting is when $x_i, y_i \in \mathbb{R}^3$, results that hold more generally will be stated in \mathbb{R}^d . The main result of this section is Theorem 2.1, which characterizes the set of solutions given by the constraints D_{ij}^* in dimension $d \leq 3$. In particular, it establishes

non-identifiability of the 3D genome structure from pairwise distance measurements in the diploid unphased setting.

THEOREM 2.1. *Let $d \leq 3$ and $n \geq 2d + 3$. Then $(x_1, \dots, x_n, y_1, \dots, y_n) \in (\mathbb{R}^d)^{2n}$ satisfies*

$$(2.1) \quad D_{ij}^* = \|x_i - x_j\|^2 + \|x_i - y_j\|^2 + \|y_i - x_j\|^2 + \|y_i - y_j\|^2 \quad \text{for all } 1 \leq i \neq j \leq n$$

if and only if it satisfies

$$(2.2) \quad x_i + y_i = x_i^* + y_i^* \quad \text{and} \quad \|x_i\|^2 + \|y_i\|^2 = \|x_i^*\|^2 + \|y_i^*\|^2 \quad \text{for all } 1 \leq i \leq n$$

up to translations and rotations in \mathbb{R}^d and permutations of x_i and y_i .

As a consequence, the measurements D_{ij}^* identify the location of each pair of homologous loci (x_i, y_i) up to a sphere with center $(x_i^* + y_i^*)/2$ and radius $\|x_i^* - y_i^*\|/2$. Namely, the points x_i, y_i lie opposite to each other anywhere on this sphere. Unless $x_i^* = y_i^*$ for all i , i.e., all spheres have radius 0, this set is infinite in dimensions $d > 1$ and hence the configuration is unidentifiable.

In the remainder of this section, we will prove [Theorem 2.1](#). The two inclusions in [Theorem 2.1](#) are proven in [Lemma 2.2](#) and [Lemma 2.4](#). In [Lemma 2.3](#) it is shown that the distance $\|x_i - y_i\|$ within each homologous pair is fixed given the pairwise distances D_{ij}^* . This result is used to prove [Lemma 2.4](#).

LEMMA 2.2. *Let $(x_1, \dots, x_n, y_1, \dots, y_n) \in (\mathbb{R}^d)^{2n}$ satisfy*

$$(2.3) \quad x_i + y_i = x_i^* + y_i^* \quad \text{and} \quad \|x_i\|^2 + \|y_i\|^2 = \|x_i^*\|^2 + \|y_i^*\|^2 \quad \text{for all } 1 \leq i \leq n.$$

Then

$$\|x_i - x_j\|^2 + \|x_i - y_j\|^2 + \|y_i - x_j\|^2 + \|y_i - y_j\|^2 = D_{ij}^* \quad \text{for all } 1 \leq i \neq j \leq n.$$

Proof. Observe that for each pair x_i, y_i satisfying the equations (2.3), it holds that

$$\begin{aligned} D_{ij}^* &= 2 \cdot (\|x_i^*\|^2 + \|y_i^*\|^2) + 2 \cdot (\|x_j^*\|^2 + \|y_j^*\|^2) - 2(x_i^* + y_i^*) \cdot (x_j^* + y_j^*) \\ &= 2 \cdot (\|x_i\|^2 + \|y_i\|^2) + 2 \cdot (\|x_j\|^2 + \|y_j\|^2) - 2(x_i + y_i) \cdot (x_j + y_j) \\ &= \|x_i - x_j\|^2 + \|x_i - y_j\|^2 + \|y_i - x_j\|^2 + \|y_i - y_j\|^2. \end{aligned}$$

This completes the proof. \square

Next we will show that the distance between homologous pairs is uniquely determined by the D_{ij}^*

LEMMA 2.3. *Let $d \leq 3$ and $n \geq 2d + 3$. Then for each $1 \leq i \leq n$ the quantity $\|x_i - y_i\|$ is identifiable from the constraints imposed by the D_{ij}^* , i.e., for any solution $(x_1, \dots, x_n, y_1, \dots, y_n) \in (\mathbb{R}^d)^{2n}$ to the equations defined by the D_{ij}^* in (2.1), the quantity $\|x_i - y_i\|$ is constant.*

The constraint $d \leq 3$ is due to our proof technique. The condition $n \geq 2d + 3$ is necessary for unique identifiability of the distance between homologous pairs of loci.

Proof. Without loss of generality we assume that $i = 1$ and show that $\|x_1 - y_1\|$ is equal to some constant. First, we perform a shift on the solution so that $x_1 = -y_1 = v$. Since shifts preserve distances, they in particular preserve the equality constraints (2.1). Hence,

$$D_{1j}^* = \|v - x_j\|^2 + \|v - y_j\|^2 + \|-v - x_j\|^2 + \|-v - y_j\|^2.$$

Expanding this out into dot products and simplifying yields

$$D_{1j}^* = 4\|v\|^2 + 2(\|x_j\|^2 + \|y_j\|^2).$$

Let $j \neq k$ be both not equal to 1. Then substituting the above leads to

$$D_{1j}^* + D_{1k}^* - D_{jk}^* = 8\|v\|^2 + 2(x_j + y_j) \cdot (x_k + y_k).$$

Defining $T_{jk} := D_{1j}^* + D_{1k}^* - D_{jk}^*$ and $s_j := \sqrt{2}(x_j + y_j)$, this is equivalent to

$$T_{jk} - 8\|v\|^2 = s_j \cdot s_k.$$

Let T' be the $(d+1) \times (d+1)$ submatrix of T satisfying $T'_{ij} = T_{i+1, j+d+2}$, i.e. the rows of T' correspond to the rows $2, 3, \dots, d+2$ of T and the columns of T' correspond to the columns $d+3, d+4, \dots, 2d+3$ of T . We now show that for generic configurations $\det(T') \neq 0$. Since $\det(T')$ can be written as a polynomial in the coordinates x_i and y_i , then $\det(T') \neq 0$ for generic configurations as long as it does not identically vanish. Hence it suffices to present one configuration where $\det(T')$ is nonzero. For $d \leq 3$ we can check this using random configurations.

Since T' has full rank, then the matrix determinant lemma implies that

$$(2.4) \quad \det(T' - 8J\|v\|^2) = (1 - 8\|v\|^2 \mathbf{1}^T (T')^{-1} \mathbf{1}) \det(T'),$$

where $\mathbf{1}$ denotes the all ones vector. Note that the scalar $\mathbf{1}^T (T')^{-1} \mathbf{1}$ is fixed and $(\det T') \neq 0$. Furthermore, since $T' - 8J\|v\|^2$ is formed from the dot products between d -dimensional vectors, it has rank at most d and therefore $\det(T' - 8J\|v\|^2) = 0$ due to $T' - 8J\|v\|^2$ being a $(d+1) \times (d+1)$ matrix. Hence, $(1 - 8\|v\|^2 \mathbf{1}^T (T')^{-1} \mathbf{1}) \det(T') = 0$, which is a linear equation in terms of $\|v\|^2$. As a consequence, it has a unique solution for $\|v\|^2$ and thus the distance between the homologous pair x_1, y_1 is fixed as long as $n \geq 2d + 3$. \square

We next characterize all solutions to the constraints imposed by the D_{ij}^* .

LEMMA 2.4. *Let $d \leq 3$ and $n \geq 2d + 3$. Let $(x_1, \dots, x_n, y_1, \dots, y_n) \in (\mathbb{R}^d)^{2n}$ be a solution to*

$$\|x_i - x_j\|^2 + \|x_i - y_j\|^2 + \|y_i - x_j\|^2 + \|y_i - y_j\|^2 = D_{ij}^* \text{ for all } 1 \leq i \neq j \leq n.$$

Then

$$x_i + y_i = x_i^* + y_i^* \text{ and } \|x_i\|^2 + \|y_i\|^2 = \|x_i^*\|^2 + \|y_i^*\|^2 \text{ for all } 1 \leq i \leq n$$

up to translations and rotations in \mathbb{R}^d and permutations of x_i and y_i .

Proof. Without loss of generality we perform a translation on the solution such that $x_1 = -y_1 = v$ for some vector v . By Lemma 2.3 the quantity $\|x_k - y_k\|$ is constant for each $1 \leq k \leq n$ and thus also $\|v\|$ is constant. Since for any $j \neq 1$ it holds that $D_{1j}^* = 4\|v\|^2 + 2(\|x_j\|^2 + \|y_j\|^2)$, also $\|x_j\|^2 + \|y_j\|^2$ is constant and hence $\|x_i\|^2 + \|y_i\|^2 = \|x_i^*\|^2 + \|y_i^*\|^2$ for all $1 \leq i \leq n$.

Similarly to the proof of Lemma 2.3, if we define $T_{jk} = D_{1j}^* + D_{1k}^* - D_{jk}^*$ and $s_j = \sqrt{2}(x_j + y_j)$, we find that

$$T_{jk} - 8\|v\|^2 = s_j \cdot s_k.$$

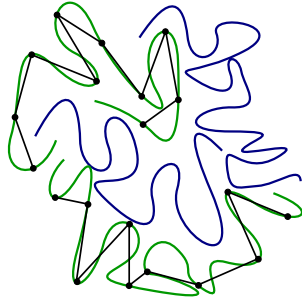


FIG. 2. *Distance constraints between neighboring beads. Green and blue curves depict two homologous pairs of chromosomes. For the green curves distances between neighboring genomic regions are shown by black lines.*

Because we have access to the diagonal constraints now, this relationship holds for all j, k and not just $j \neq k$. Thus $T - 8J\|v\|^2$ is a symmetric $(n - 1) \times (n - 1)$ matrix admitting a rank d factorization. Let S be the matrix formed with the vectors s_j . We then have $T - 8J\|v\|^2 = SS^T$. There is a result on rank factorizations of symmetric matrices that any other factorization $T - 8J\|v\|^2 = S'S'^T$ satisfies $S = S'Q$ for some orthogonal matrix Q [22, Proposition 3.2]. Thus for any other solution s'_j , we have $s_j = s'_jQ$, implying all solutions are simply orthogonal transformations of each other (rotations, reflections, etc.)

In summary, we have shown that once we have fixed $x_1 + y_1 = 0$ via translation, then the quantities $x_j + y_j$ are unique up to orthogonal transformations and the quantities $\|x_j\|^2 + \|y_j\|^2$ are unique. \square

3. Distance constraints between neighboring loci. In section 2, we showed that the 3D genome configuration is not identifiable from pairwise distance constraints available from typical (unphased) contact frequency maps. In order to gain identifiability, we next consider adding other biological constraints to the problem formulation that are generally available or can be measured. In particular, since DNA can be viewed as a string of connected beads, we use the distance between adjacent beads as an additional constraint. The distance between neighboring beads can be derived empirically for example from imaging studies [29, 21]; see also our experimental results in section 6. The additional mathematical constraints are:

$$\|x_i - x_{i+1}\| = \|x_i^* - x_{i+1}^*\| \text{ and } \|y_i - y_{i+1}\| = \|y_i^* - y_{i+1}^*\| \text{ for } 1 \leq i \leq n - 1,$$

where $x_1^*, x_2^*, \dots, x_n^*$ and $y_1^*, y_2^*, \dots, y_n^*$ correspond to consecutive beads on homologous chromosomes; see Figure 2.

In this section we show the following results: under the additional distance constraints between neighboring loci, we prove that identifiability can be obtained in the 2D setting (Proposition 3.1). However, in the 3D setting we prove that there are still infinitely many 3D configurations even with these additional distance constraints (Proposition 3.2).

For the proofs of Proposition 3.1 and Proposition 3.2 we recall from Theorem 2.1 that (x_i, y_i) and (x_i^*, y_i^*) are diametrically opposite points on the same sphere. Denote the i -th sphere by S_i and let it have center c_i and radius r_i . Then $\|c_i - x_i\| = r_i$ and $2c_i - x_i = y_i$.

PROPOSITION 3.1. *For $n \geq 3$ and generic $(x_1^*, \dots, x_n^*, y_1^*, \dots, y_n^*) \in (\mathbb{R}^2)^{2n}$, there*

is a unique point $(x_1, \dots, x_n, y_1, \dots, y_n) \in (\mathbb{R}^2)^{2n}$ satisfying the equations

$$(3.1) \quad \begin{aligned} x_i + y_i &= x_i^* + y_i^* \text{ and } \|x_i\|^2 + \|y_i\|^2 = \|x_i^*\|^2 + \|y_i^*\|^2 \text{ for } 1 \leq i \leq n, \\ \|x_i - x_{i+1}\| &= \|x_i^* - x_{i+1}^*\| \text{ and } \|y_i - y_{i+1}\| = \|y_i^* - y_{i+1}^*\| \text{ for } 1 \leq i \leq n-1. \end{aligned}$$

Proof. We have $y_1 = 2c_1 - x_1$ and $y_2 = 2c_2 - x_2$. Plugging this into $\|y_1 - y_2\| = \|y_1^* - y_2^*\|$ gives

$$\begin{aligned} \|y_1^* - y_2^*\| &= \|(2c_1 - x_1) - (2c_2 - x_2)\|^2 \\ &= \|(2c_1 - 2c_2) - (x_1 - x_2)\|^2 \\ &= \|2c_1 - 2c_2\|^2 + \|x_1 - x_2\|^2 - 2(2c_1 - 2c_2) \cdot (x_1 - x_2). \end{aligned}$$

The quantities $\|2c_1 - 2c_2\|^2$ and $\|x_1 - x_2\|^2$ are fixed. This implies that the quantity $(2c_1 - 2c_2) \cdot (x_1 - x_2)$ is fixed. Since we know $\|x_1 - x_2\|$ and $c_1 \neq c_2$ holds by genericness, then there are two possible angles for $x_1 - x_2$ (this is where we use the 2D constraint) and thus that there are two possible solutions for $x_1 - x_2$.

Because x_1, x_2 are constrained to lie on circles, the solutions for x_1 are the intersection points of the first circle and the second circle translated by $x_1 - x_2$ and the solutions for x_2 are the intersection points of the second circle and the first circle translated by $x_2 - x_1$. Hence each solution for $x_1 - x_2$ leads to at most two possible solutions for (x_1, x_2) . In turn this implies there are at most four solutions for x_2 .

We now investigate the four solutions. The first two solutions are obtained by translating the circle centered at c_1 by $x_2^* - x_1^*$ and intersecting it with the circle centered at c_2 , see [Figure 3](#). One of the two solutions is x_2^* . The other two solutions are reflections of these two solutions over the line from c_1 to c_2 .

Let x_1^*, x_2^*, c_1, c_2 be fixed. They determine four possible solutions for x_2 . We will show that these four solutions are different from the four solutions we get from considering x_2^*, x_3^*, c_2, c_3 for generic x_3^*, c_3 (apart from x_2^*).

If either of the reflected solutions over the line from c_2 to c_3 coincides with one of the four original solutions, then we can perturb c_3 away from the line from c_2 to c_3 to change these solutions. If the solution that is the intersection point of the circle centered at c_2 and the translation by $x_2^* - x_3^*$ of the circle centered at c_3 (different from x_2^*) coincides with one of the four original solutions, then we can perturb x_3^* .

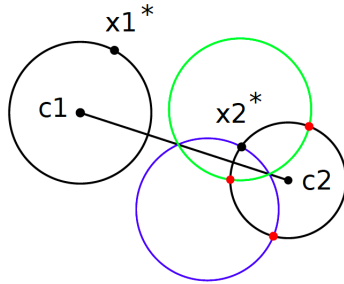


FIG. 3. *Identifiability in the 2D setting with neighboring distance constraints. Two solutions for x_2 are obtained by translating the circle centered at c_1 by $x_2^* - x_1^*$ (this new circle is colored blue) and intersecting it with the circle centered at c_2 . The other two solutions are obtained by reflecting the blue circle over the line through c_1 and c_2 (this new circle is colored green) and intersecting it with the circle centered at c_2 . The true solution for x_2 is colored black and the three alternative solutions for x_2 are colored red.*

This changes $x_2^* - x_3^*$ and hence the second intersection point of the circle centered at c_2 and the translation by $x_2^* - x_3^*$ of the circle centered at c_3 .

A similar argument can be used to show that x_3, \dots, x_{n-1} have unique solutions. Given a unique solution for x_2 , there are two solutions for x_1 if and only if x_2^* lies on the line from c_1 to c_2 . This is however not a generic configuration. A similar argument applies for x_n . \square

Despite having uniqueness in 2D, we do not have uniqueness in 3D as shown in the following proposition.

PROPOSITION 3.2. *Let $n \in \mathbb{N}$. For generic $(x_1^*, \dots, x_n^*, y_1^*, \dots, y_n^*) \in (\mathbb{R}^3)^{2n}$, there are infinitely many points $(x_1, \dots, x_n, y_1, \dots, y_n) \in (\mathbb{R}^3)^{2n}$ satisfying equations (3.1).*

Proof. If $n = 1$, then x_1^*, y_1^* can be chosen randomly with the constraint that $x_1^* \neq y_1^*$. Then x_1 and y_1 can be any points on the sphere S_1 defined by x_1^*, y_1^* . Now assume that $n \geq 2$. Fix any x_1^*, y_1^* such that $x_1^* \neq y_1^*$. Choose two circles C_1 and C'_1 on the sphere S_1 defined by x_1^*, y_1^* that intersect at two points one of which is x_1^* . The circle C_1 is the intersection of S_1 and another sphere T_1 . Let x_2^* be the center of the sphere T_1 . Let C''_1 be the circle on S_1 that consists of points antipodal to C'_1 . Then C''_1 is also an intersection of S_1 and another sphere T''_1 . Let y_2^* be the center of the sphere T''_1 . We use the same procedure to construct x_3^* and y_3^* from x_2^* and y_2^* , x_4^* and y_4^* from x_3^* and y_3^* etc.

The only condition on x_1^* and y_1^* is $x_1^* \neq y_1^*$, hence (x_1^*, y_1^*) is a generic point in $\mathbb{R}^3 \times \mathbb{R}^3$. The condition that C_1 is a circle on the sphere S_1 containing x_1^* is equivalent to x_2^* being any point in \mathbb{R}^3 outside the line through x_1^* and y_1^* . Similarly, the condition that C'_1 is a circle on the sphere S_1 containing x_1^* is equivalent to y_2^* being any point in \mathbb{R}^3 outside the line through x_1^* and y_1^* . The condition that C_1 and C'_1 intersect at two different points of S_1 is equivalent to the normal vector of the tangent plane of S_1 at x_1^* and the normal vectors of the planes defined by C_1 and C'_1 being linearly independent. Hence $(x_1^*, x_2^*, y_1^*, y_2^*)$ is a generic point in $(\mathbb{R}^3)^4$. Similar arguments can be used to show that $(x_1^*, x_2^*, \dots, x_n^*, y_1^*, y_2^*, \dots, y_n^*)$ is a generic point in $(\mathbb{R}^3)^{2n}$.

Now consider points x_n and y_n in an ε -neighborhood of x_n^* and y_n^* . Consider the spheres that are centered at x_n and y_n and have radii $\|x_{n-1}^* - x_n^*\|$ and $\|y_{n-1}^* - y_n^*\|$. The intersections of these spheres with S_{n-1} give circles \tilde{C}_{n-1} and \tilde{C}''_{n-1} that are perturbations of circles C_{n-1} and C''_{n-1} . In particular, the intersection of the circle \tilde{C}_{n-1} and the circle \tilde{C}''_{n-1} that consists of points antipodal to \tilde{C}_{n-1} consists of two points for ε small enough. Choosing x_{n-1} to be the intersection point corresponding to x_{n-1}^* and y_{n-1} its antipodal gives points x_{n-1}, y_{n-1} satisfying $\|x_{n-1} - x_n\| = \|x_{n-1}^* - x_n^*\|$ and $\|y_{n-1} - y_n\| = \|y_{n-1}^* - y_n^*\|$.

Assuming that ε is small enough, then x_{n-1} and y_{n-1} are in small neighborhoods of x_{n-1}^* and y_{n-1}^* , and we can continue the same procedure to find x_{n-2} and y_{n-2} from x_{n-1} and y_{n-1} , x_{n-3} and y_{n-3} from x_{n-2} and y_{n-2} etc. In particular, we can find $x_1, \dots, x_{n-1}, y_1, \dots, y_{n-1}$ satisfying equations (3.1) for every x_n and y_n in an ε -neighborhood of x_n^* and y_n^* . \square

The previous proposition suggests that there are two degrees of freedom for choosing $x_1, \dots, x_n, y_1, \dots, y_n$ on each homologous pair and thus that finite identifiability requires two additional algebraically independent constraints per homologous pair. Similarly this suggests that unique identifiability requires three additional algebraically independent constraints per homologous pair, where each endpoint of a chromosome needs to be included in at least one of the additional constraints.

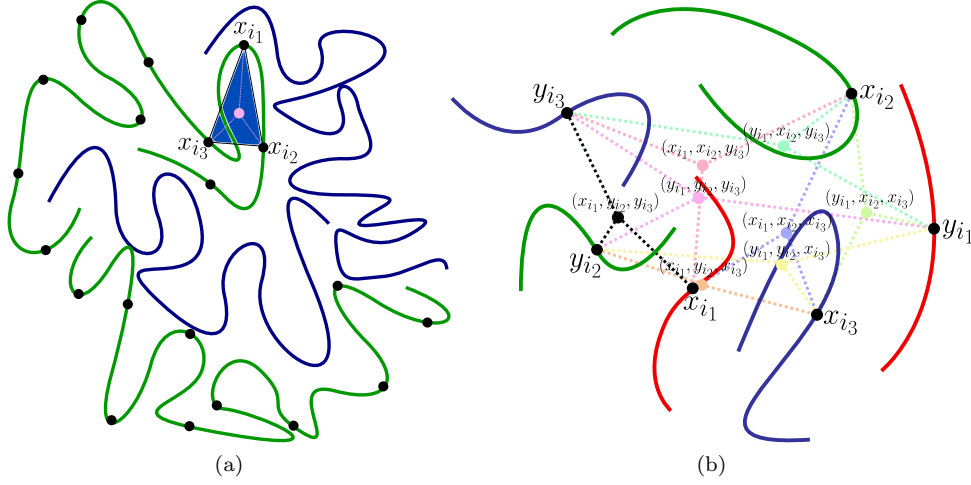


FIG. 4. Higher-order distance constraints. (a) Three loci $x_{i_1}, x_{i_2}, x_{i_3}$, located on the same chromosome, are depicted. In the phased setting, the higher-order distance $D_{x_{i_1} x_{i_2} x_{i_3}}$ is defined as the sum of the distances (pink dashed lines) of the three loci $x_{i_1}, x_{i_2}, x_{i_3}$ to their centroid (pink point). Green and blue curves depict two different chromosomes. (b) Illustrates the definition of $D_{i_1 i_2 i_3}$ in the unphased setting. Green, blue and red curves depict neighborhoods around three homologous loci $(x_{i_1}, y_{i_1}), (x_{i_2}, y_{i_2})$ and (x_{i_3}, y_{i_3}) . From these homologous loci 8 possible higher-order distances can be defined (colored dashed lines) based on the 8 centroids depicted in the figure. The higher-order distance $D_{i_1 i_2 i_3}$ is defined as the minimum of these 8 distances (achieved here by the three black dashed line segments).

4. Identifiability from higher-order contact constraints. In section 3, we showed that considering distances between neighboring beads only yields identifiability in 2D but not in 3D. In the following, we consider adding further constraints that are becoming widely available from experimental data, namely higher-order contact frequencies between three or more loci as measured by experimental assays such as SPRITE [33], C-walks [31] and GAM [2]. We express these constraints mathematically by letting $F \in \mathbb{R}^{m \times m \times \dots \times m}$ be a contact frequency tensor, where $F_{x_{i_1}, x_{i_2}, \dots, x_{i_k}}$ measures the contact frequency between loci i_1, i_2, \dots, i_k with coordinates $x_{i_1}, x_{i_2}, \dots, x_{i_k}$. In the unphased setting, we can only measure a combination of contact frequencies over the homologous loci $\{x_{i_1}, y_{i_1}\} \times \{x_{i_2}, y_{i_2}\} \times \dots \times \{x_{i_k}, y_{i_k}\}$, which we denote by $F_{i_1 i_2 \dots i_k}$. In addition, as for 2-way interactions, we turn contact frequencies into “distances” by defining $D_{i_1 i_2 \dots i_k} := 1/F_{i_1 i_2 \dots i_k}$.

In the following, we provide our interpretation of distances in the higher-order setting. For simplicity, we first describe the higher-order distances for three loci in the phased setting. Since $F_{x_{i_1} x_{i_2} x_{i_3}}$ counts how often the three loci come together, we interpret $D_{x_{i_1} x_{i_2} x_{i_3}}$ as the sum of the distances of the three loci $x_{i_1}, x_{i_2}, x_{i_3}$ to their centroid (Figure 4a). We next provide a generalization to the unphased setting. For three homologous loci $(x_{i_1}, y_{i_1}), (x_{i_2}, y_{i_2})$ and (x_{i_3}, y_{i_3}) , their contact frequency can be formed by 8 possible triples, namely $(x_{i_1}, x_{i_2}, x_{i_3}), (x_{i_1}, x_{i_2}, y_{i_3}), (x_{i_1}, y_{i_2}, x_{i_3}), (y_{i_1}, x_{i_2}, x_{i_3}), (x_{i_1}, y_{i_2}, y_{i_3}), (y_{i_1}, y_{i_2}, x_{i_3}), (y_{i_1}, x_{i_2}, y_{i_3})$, and $(y_{i_1}, y_{i_2}, y_{i_3})$. We will assume that one of the triples constitutes the majority of the observed contact frequency count and hence we define $D_{i_1 i_2 i_3}$ as the minimum over all 8 higher order distances. This is illustrated in Figure 4b. Generalizing from three to k loci, our higher-order

distance definition then becomes

$$D_{i_1 i_2 \dots i_k} = \min_{z_{i_j} \in \{x_{i_j}, y_{i_j}\}} \left(\sum_{j=1}^k \|z_{i_j} - (z_{i_1} + \dots + z_{i_k})/k\|^2 \right).$$

In the following, we prove our main result; namely we show that the distance constraints of order 3 (3-way distances) together with the previously considered pairwise distance constraints and distance constraints among consecutive beads results in unique identifiability of the 3D genome configuration ([Theorem 4.1](#)). In fact, only very few order 3 distance constraints are required for unique identifiability. As we show in [Theorem 4.1](#) it is sufficient that the first and last bead of each chromosome be contained in an order 3 distance constraint. This is a reasonable constraint given that methods such as SPRITE, C-walks and GAM measure higher-order interactions over the whole genome. These insights are of interest experimentally since they suggest that the methods can restrict the measurement of such higher order constraints to first and last beads of each chromosome, known as telomeres.

THEOREM 4.1. *Let m be the number of chromosome pairs, let n_1, n_2, \dots, n_m be the number of domains on chromosomes $1, 2, \dots, m$ and define $n = n_1 + n_2 + \dots + n_m$. Let $I \subseteq [n] \times [n] \times [n]$ be such that each of $1, n_1, n_1 + 1, n_1 + n_2, \dots, n_1 + n_2 + \dots + n_{m-1} + 1, n$ (labels of domains at the beginning and at the end of each chromosome) is contained in at least one triple in I . Let $x_1^*, \dots, x_n^*, y_1^*, \dots, y_n^* \in \mathbb{R}^3$ be fixed such that*

$$\min_{z_i^* \in \{x_i^*, y_i^*\} \text{ for } i=k_1, k_2, k_3} \left(\sum_{j \in \{k_1, k_2, k_3\}} \|z_j^* - (z_{k_1}^* + z_{k_2}^* + z_{k_3}^*)/3\|^2 \right) = 0$$

for $(k_1, k_2, k_3) \in I$.

Consider the polynomial system:

$$(4.1) \quad \begin{aligned} & x_i + y_i = x_i^* + y_i^* \text{ and } \|x_i\|^2 + \|y_i\|^2 = \|x_i^*\|^2 + \|y_i^*\|^2 \text{ for } 1 \leq i \leq n, \\ & \|x_i - x_{i+1}\| = \|x_i^* - x_{i+1}^*\| \text{ and } \|y_i - y_{i+1}\| = \|y_i^* - y_{i+1}^*\| \\ & \text{for } i \in [n] \setminus \{n_1, n_1 + n_2, \dots, n\}, \\ & \min_{z_i \in \{x_i, y_i\} \text{ for } i=k_1, k_2, k_3} \left(\sum_{j \in \{k_1, k_2, k_3\}} \|z_j - (z_{k_1} + z_{k_2} + z_{k_3})/3\|^2 \right) = 0 \\ & \text{for } (k_1, k_2, k_3) \in I. \end{aligned}$$

Then for generic $x_1^*, \dots, x_n^*, y_1^*, \dots, y_n^*$, this system has a unique solution in $(\mathbb{R}^3)^{2n}$.

To prove [Theorem 4.1](#), we will need two lemmas. [Lemma 4.2](#) states that for a fixed solution (x_1^*, y_1^*) on a sphere S_1 and given distances between solutions on S_1 and S_2 , there are finitely many solutions (x_2, y_2) on the sphere S_2 . [Lemma 4.3](#) is an extension of [Lemma 4.2](#). It states that if one has finitely many solutions on a sphere S_i , then given distances between neighboring beads, there are finitely many solutions on any sphere connected to S_i .

LEMMA 4.2. *Let $x_1^*, x_2^*, y_1^*, y_2^* \in \mathbb{R}^3$ be fixed. Consider the polynomial system:*

$$(4.2) \quad \begin{aligned} & x_2 + y_2 = x_2^* + y_2^*, \|x_2\|^2 + \|y_2\|^2 = \|x_2^*\|^2 + \|y_2^*\|^2, \\ & \|x_1^* - x_2\| = \|x_1^* - x_2^*\| \text{ and } \|y_1^* - y_2\| = \|y_1^* - y_2^*\|. \end{aligned}$$

For generic $x_1^*, x_2^*, y_1^*, y_2^*$, this system has finitely many solutions in $(\mathbb{R}^3)^{2n}$.

Proof. The first two equations of (4.2) say that x_2, y_2 and x_2^*, y_2^* are pairs of antipodal points on the same sphere. We denote this sphere by S_2 . The third equation says that x_2 is the same distance from x_1^* as x_2^* is from x_1^* . Hence x_2 must lie on the circle C_{x_2} that is the intersection of S_2 and the sphere centered at x_1^* and with radius $\|x_1^* - x_2^*\|$. The last equation says that y_2 must lie on the circle C_{y_2} that is the intersection of S_2 and the sphere centered at y_1^* with radius $\|y_1^* - y_2^*\|$. We consider the circle C'_{x_2} that consists of antipodal points to the circle C_{y_2} on the sphere S_2 . The intersection of the circles C_{x_2} and C'_{x_2} gives the solutions for x_2 . Unless the two circles are equal, they intersect at at most two points. Since y_2 is antipodal to x_2 , then for each x_2 there is a unique y_2 . The circles coincide if and only if x_1^*, y_1^* and the center of S_2 are collinear. \square

LEMMA 4.3. Let $x_1^*, \dots, x_n^*, y_1^*, \dots, y_n^* \in \mathbb{R}^3$ be fixed. Consider the polynomial system:

$$\begin{aligned} x_i + y_i &= x_i^* + y_i^* \text{ and } \|x_i\|^2 + \|y_i\|^2 = \|x_i^*\|^2 + \|y_i^*\|^2 \text{ for } 2 \leq i \leq n, \\ \|x_1^* - x_2\| &= \|x_1^* - x_2^*\|, \|y_1^* - y_2\| = \|y_1^* - y_2^*\|, \\ \|x_i - x_{i+1}\| &= \|x_i^* - x_{i+1}^*\| \text{ and } \|y_i - y_{i+1}\| = \|y_i^* - y_{i+1}^*\| \text{ for } 2 \leq i \leq n-1. \end{aligned}$$

For generic $x_1^*, \dots, x_n^*, y_1^*, \dots, y_n^*$, this system has finitely many solutions in $(\mathbb{R}^3)^{2n-2}$.

Proof. By Lemma 4.2, there are finitely many antipodal pairs $(x_2, y_2) \in \mathbb{R}^3 \times \mathbb{R}^3$ on S_2 such that $\|x_1^* - x_2\| = \|x_1^* - x_2^*\|$ and $\|y_1^* - y_2\| = \|y_1^* - y_2^*\|$. Similarly, for each of these antipodal pairs $(x_2, y_2) \in \mathbb{R}^3 \times \mathbb{R}^3$ on S_2 , there are finitely many antipodal pairs $(x_3, y_3) \in \mathbb{R}^3 \times \mathbb{R}^3$ on S_3 satisfying $\|x_2 - x_3\| = \|x_2^* - x_3^*\|$ and $\|y_2 - y_3\| = \|y_2^* - y_3^*\|$ etc. \square

Proof of Theorem 4.1. We recall that the first line of the polynomial system (4.1) gives that x_i, y_i are antipodal points on a sphere S_i . Consider a triple $(k_1, k_2, k_3) \in I$ that contains 1 and the equation on the last line of the polynomial system (4.1) corresponding to this triple. This equation gives that $z_{k_1}, z_{k_2}, z_{k_3}$, where $z_i \in \{x_i, y_i\}$, coincide. Hence $z_{k_1}, z_{k_2}, z_{k_3}$ lie on the intersection of $S_{k_1}, S_{k_2}, S_{k_3}$. Generically, if the intersection of three spheres is non-empty in \mathbb{R}^3 , then it consists of two points P and P' . This gives four possible solutions for x_1, y_1 : the points P, P' and their antipodals on S_1 . By Lemma 4.3, there are finitely many solutions for $x_2, \dots, x_{n_1}, y_2, \dots, y_{n_1}$ given these fixed solutions x_1, y_1 on S_1 . In the next two paragraphs we will show that generically these finitely many solutions do not contain antipodal points on any of the spheres S_2, \dots, S_{n_1} .

If there are two antipodal solutions on S_i , then we may assume that they come either from the same solution on S_1 or antipodal solutions on S_1 , because we can perturb $S_{k_1}, S_{k_2}, S_{k_3}$ slightly to change the other pair of solutions. First we will show that generically a solution for x_i on S_i does not give a pair of antipodal solutions for x_{i+1} on S_{i+1} . If this was the case, then both the solution for x_i and its antipodal would have to lie on the plane that is perpendicular to the line through the antipodal pair of solutions for x_{i+1} on S_{i+1} . This plane contains the centers of S_i and S_{i+1} . Hence for a solution for x_i , there is only one antipodal pair on solutions on S_{i+1} . Thus for a generic distance between the solutions on S_i and S_{i+1} , a solution on S_i does not give an antipodal pair of solutions on S_{i+1} .

Secondly, suppose that two different solutions on S_i give a pair of antipodal solutions on S_{i+1} . We will show that when we perturb the distance between solutions

on S_i and S_{i+1} , then we do not get an antipodal pair anymore. Let x_i and x'_i be two different solutions on S_i that give solutions x_{i+1} and $2c_{i+1} - x_{i+1}$ on S_{i+1} . Hence $\|2c_{i+1} - x_{i+1} - x'_i\|^2 = \|x_{i+1} - x_i\|^2$. We want to show that generically

$$\|2c_{i+1} - (x_{i+1} + \epsilon) - x'_i\|^2 \neq \|x_{i+1} + \epsilon - x_i\|^2,$$

where $x_{i+1} + \epsilon$ is the perturbed solution. Indeed, using the identity $\|x_{i+1} - x_i\|^2 = \|2c_{i+1} - x_{i+1} - x'_i\|^2$ gives

$$\|2c_{i+1} - (x_{i+1} + \epsilon) - x'_i\|^2 - \|x_{i+1} + \epsilon - x_i\|^2 = 2\epsilon(x_i + x'_i - 2c_{i+1}).$$

This quantity is equal to zero if and only if $\epsilon = 0$ or c_{i+1} is the middle point of the line segment from x_i to x'_i . This is generically not the case.

Using a triple $(k'_1, k'_2, k'_3) \in I$ containing n_1 and the equation for this triple, we get four possible solutions for x_{n_1}, y_{n_1} . Generically, only one of them coincides with the finitely many solutions on S_{n_1} that we get from the solutions on S_1 , because perturbing the spheres slightly (with keeping the coinciding points fixed) perturbs the second intersection point of the three spheres and we know that generically the finitely many points do not contain antipodal points.

The unique solution on S_n comes from one solution on each of the spheres S_1, \dots, S_{n-1} : If this was not the case then two different solutions on S_i give the same solution on S_{i+1} . By the proof of [Proposition 3.1](#), the dot product $(c_i - c_{i+1}) \cdot (x_i - x_{i+1})$ is fixed. Hence for a fixed x_{i+1} , all possible solutions for x_i lie on a hyperplane and this hyperplane is perpendicular to $c_i - c_{i+1}$. Therefore, if two solutions on S_i give the same solution on S_{i+1} , then they lie on a hyperplane perpendicular to $c_i - c_{i+1}$. By slightly perturbing the sphere S_{i+1} , this is not the case anymore, and hence generically a solution on S_{i+1} comes from a unique solution on S_i . \square

5. Algorithms and implementation. So far, we derived a theoretical framework to establish when we have unique and finite identifiability of the 3D configuration in the noiseless setting. However, a unique solution does not necessarily mean that we can find it efficiently, as in many cases finding the solution may be NP-hard. In addition, we have so far not yet considered the noisy setting. In this section, we show how to construct an optimization formulation to determine the 3D configuration efficiently.

We frame the 3D reconstruction problem as a Euclidean embedding problem, where the coordinates $x_1, \dots, x_n, y_1, \dots, y_n \in \mathbb{R}^3$ are inferred from distances. Similar to ChromSDE [\[46\]](#), we formulate all distances in terms of entries in the Gram matrix G , which tracks the dot products between the $2n$ genomic regions. Namely, letting the column/row i of G correspond to x_i and the column/row $n+i$ correspond to its homologous locus y_i , then the distances are given by $\|x_i - x_j\|^2 = G_{i,i} + G_{j,j} - 2G_{i,j}$, $\|x_i - y_j\|^2 = G_{i,i} + G_{n+j,n+j} - 2G_{i,n+j}$ and $\|y_i - y_j\|^2 = G_{n+i,n+i} + G_{n+j,n+j} - 2G_{n+i,n+j}$. It is natural to work with the Gram matrix G , since it is rotation invariant. By imposing the constraint $\sum_{i,j} G_{i,j} = 0$ we can also fix the translational axis. Also the additional distance constraints that we introduced in the previous sections ([Theorem 2.1](#), [Proposition 3.1](#), [Theorem 4.1](#)) can be represented as linear constraints in terms of entries in G as follows:

- Pairwise distances:

$$g_{ij}(G) := G_{i,i} + G_{j,j} + G_{n+i,n+i} + G_{n+j,n+j} - G_{i,j} - G_{n+i,j} - G_{i,n+j} - G_{n+i,n+j}$$

- Distances between homologous pairs:

$$g_{ii}(G) := G_{i,i} + G_{n+i,n+i} - 2G_{i,n+i}$$

- Distances between neighboring beads:

$$g_{i+}(G) := G_{i,i} + G_{i+1,i+1} - 2G_{i,i+1}$$

- Distances of order 3 (can be generalized to higher orders):

$$g_{ijk}(G) := \min_l (g_{ijkl} : l = 1, \dots, 8)$$

where

$$\begin{aligned} g_{ijk1}(G) &:= G_{i,i} + G_{j,j} + G_{k,k} - G_{i,j} - G_{i,k} - G_{j,k}, \\ g_{ijk2}(G) &:= G_{i,i} + G_{j,j} + G_{n+k,n+k} - G_{i,j} - G_{i,n+k} - G_{j,n+k}, \\ g_{ijk3}(G) &:= G_{i,i} + G_{n+j,n+j} + G_{k,k} - G_{i,n+j} - G_{i,k} - G_{n+j,k}, \\ g_{ijk4}(G) &:= G_{i,i} + G_{n+j,n+j} + G_{n+k,n+k} - G_{i,n+j} - G_{i,n+k} - G_{n+j,n+k}, \\ g_{ijk5}(G) &:= G_{n+i,n+i} + G_{j,j} + G_{k,k} - G_{n+i,j} - G_{n+i,k} - G_{j,k}, \\ g_{ijk6}(G) &:= G_{n+i,n+i} + G_{j,j} + G_{n+k,n+k} - G_{n+i,j} - G_{n+i,n+k} - G_{j,n+k}, \\ g_{ijk7}(G) &:= G_{n+i,n+i} + G_{n+j,n+j} + G_{k,k} - G_{n+i,n+j} - G_{n+i,k} - G_{n+j,k}, \\ g_{ijk8}(G) &:= G_{n+i,n+i} + G_{n+j,n+j} + G_{n+k,n+k} \\ &\quad - G_{n+i,n+j} - G_{n+i,n+k} - G_{n+j,n+k}. \end{aligned}$$

Our objective is to determine a rank 3 solution of G , satisfying the above constraints. However, this optimization problem is non-convex due to the rank constraint, and we instead consider the standard relaxation: we minimize the trace of the Gram matrix as an approximation to matrix rank [17]. The resulting optimization problem then becomes the following semidefinite program (SDP):

$$\begin{aligned} (5.1) \quad & \underset{G}{\text{minimize}} && \text{tr}(G) \\ & \text{subject to} && g_{ii}(G) = D_{ii}^*, \quad 1 \leq i \leq n, \\ & && g_{ij}(G) = D_{ij}^*, \quad 1 \leq i < j \leq n, \\ & && g_{i+}(G) = D_{i+}^*, \quad i \in \Omega_1, \\ & && g_{ijk}(G) = D_{ijk}^*, \quad (i, j, k) \in \Omega_2, \\ & && \sum_{1 \leq i, j \leq 2n} G_{i,j} = 0, \\ & && G \succeq 0. \end{aligned}$$

Here, D_{ii}^* denote the distances between homologous pairs computed from the pairwise distances using Lemma 2.3, D_{ij}^* denote the pairwise distances, D_{i+}^* denote the distances between neighboring beads, and D_{ijk}^* denote the distances between three loci (while one could also consider 4 or higher order distance constraints, in our implementation we only used 3-way distance constraints since higher-order contacts are extremely sparse). The index set $\Omega_1 = [2n] \setminus \{n_1, n_1+n_2, \dots, n, n+n_1, n+n_1+n_2, \dots, 2n\}$ corresponds to all beads that are not the last bead on a chromosome. The index set $\Omega_2 \subseteq [n]^3$ corresponds to all triples of beads with non-zero contact frequencies.

In the noisy setting, which is relevant for biological data, we replace the equality constraints by penalties in the loss function. Namely, using D^* for the noiseless and D for the noisy distances, we replace the equality constraints of the form $g(G) = D^*$ by

adding $(g(G) - D)^2$ to the objective function. For the higher-order distance constraints of the form $D_{ijk}^* = \min(g_{ijk1}(G), \dots, g_{ijk8}(G))$ for $(i, j, k) \in \Omega_2$ we use slack variables and a convex relaxation using an atomic norm that combines the ℓ_2 - and ℓ_1 -norms. More precisely, we propose the use of the following transformation in the noisy setting,

$$D_{ijk} + \lambda_{ijkl} = g_{ijkl}(G) + s_{ijkl} \text{ for } l = 1, 2, \dots, 8,$$

where $\lambda_{ijkl}, s_{ijkl} \geq 0$ for all i, j, k, l act as slack variables. In general, for each triple (i, j, k) we want one of the λ_{ijkl} to be close to 0 and the sum over all s_{ijkl} to be small. Naively this can be done by placing $\sum s_{ijkl} + \sum \lambda_{ijkl}$ into the objective function. However, this would not enforce for each (i, j, k) at least one λ_{ijkl} to be close to 0. Instead we propose to use

$$\sum_{(i,j,k) \in \Omega_2, 1 \leq l \leq 8} s_{ijkl} + \sqrt{\sum_{(i,j,k) \in \Omega_2} \left(\sum_{1 \leq l \leq 8} \lambda_{ijkl} \right)^2}.$$

The ℓ_2 -norm will push down the $\sum_l \lambda_{ijkl}$ for each (i, j, k) , while the ℓ_1 norm will drive at least one of the λ_{ijkl} to zero, which is precisely the desired behavior. The quantity $\sqrt{\sum_{i,j,k} (\sum_l \lambda_{ijkl})^2}$ is an atomic norm as defined in [6] with the set of atoms

$$\begin{aligned} \mathcal{A} = \{(\lambda_{ijkl}) : \sum_{i,j,k} \left(\sum_l \lambda_{ijkl} \right)^2 = 1 \text{ and} \\ \sum_{i,j,k} \lambda_{ijkl}^2 = 1 \text{ for } l_{ijk} = 1, \dots, 8, (i, j, k) \in \Omega_2\}. \end{aligned}$$

Then the optimization problem in the noisy setting becomes:

$$\begin{aligned} (5.2) \quad \underset{G, s, \lambda}{\text{minimize}} \quad & \rho \operatorname{tr}(G) + \sum_{1 \leq i \leq n} (g_{ii}(G) - D_{ii})^2 + \sum_{1 \leq i < j \leq n} (g_{ij}(G) - D_{ij})^2 \\ & + \sum_{i \in \Omega_1} (g_{i+}(G) - D_{i+})^2 + \sum_{(i,j,k) \in \Omega_2, 1 \leq l \leq 8} s_{ijkl} \\ & + \sqrt{\sum_{(i,j,k) \in \Omega_2} \left(\sum_{1 \leq l \leq 8} \lambda_{ijkl} \right)^2} \\ \text{subject to} \quad & D_{ijk} + \lambda_{ijkl} = g_{ijkl}(G) + s_{ijkl}, (i, j, k) \in \Omega_2, 1 \leq l \leq 8, \\ & s_{ijkl} \geq 0, (i, j, k) \in \Omega_2, 1 \leq l \leq 8, \\ & \lambda_{ijkl} \geq 0, (i, j, k) \in \Omega_2, 1 \leq l \leq 8, \\ & \sum_{1 \leq i, j \leq 2n} G_{i,j} = 0, \\ & G \succeq 0. \end{aligned}$$

We use a tuning parameter ρ for the trace in the objective function, which can be used to balance obtaining a low-rank solution versus satisfying the constraints. The tuning parameter ρ can be chosen using cross-validation or by selecting it so that the resulting solution has small $(d+1)^{\text{th}}$ eigenvalue. As shown in [section SM3](#) and [section](#)

SM7, we observe on synthetic and real data that the solution is robust to the choice of ρ .

The theoretical results from Lemma 2.3 allow us to compute the distances between homologous pairs from the pairwise distances D_{ij} . We recall that we need to compute $\|v\|^2$ such that

$$\det(T' - 8J\|v\|^2) = 0,$$

where T' is an invertible matrix constructed from the pairwise distance matrix by selecting a set of $2d+2$ indices. One step of computing $\|v\|$ involves inverting T' . Even if the error in the measurements is small, noise can propagate and severely impact this computation. In order to obtain a robust estimate of homolog-homolog distances, for each locus i , we sample 100 T' matrices and obtain 100 solutions to the equation for $\|v\|^2$. We then take the median of the solutions to be the homolog-homolog distance for locus i and use these homolog-homolog distances for the evaluation of our algorithms on synthetic and real data in the following section.

To solve the two convex optimization problems presented in this section for the noiseless and noisy setting, we make use of the solver MOSEK implemented in CVX within MATLAB. This results in the Gram matrix. In order to reconstruct the coordinates of the genomic regions from the Gram matrix, we use an eigenvector decomposition as also done in [46], namely: letting $\gamma_1, \dots, \gamma_d$ be the top d eigenvalues and ν_1, \dots, ν_d the corresponding eigenvectors of G , then

$$x_i = (\sqrt{\gamma_1} \cdot \nu_{1,i}, \dots, \sqrt{\gamma_d} \cdot \nu_{d,i}) \text{ and } y_i = (\sqrt{\gamma_1} \cdot \nu_{1,n+i}, \dots, \sqrt{\gamma_d} \cdot \nu_{d,n+i}) \text{ for } i = 1, \dots, n.$$

Since we are interested in recovering the genome configuration in 3D, we use $d = 3$, thereby obtaining the desired 3D diploid configuration. We provide the code for our algorithm at <https://github.com/uhlerlab/diploid-3D-reconstruction>.

6. Evaluation on synthetic and real data.

6.1. Synthetic data. We start by testing our method on simulated data. For this we construct three different types of 3D structures: (a) a Brownian motion model using a standard normal distribution to generate successive points; (b) points sampled uniformly along a spiral with random translations sampled uniformly within $(0, 0.5)$ range and orientations sampled uniformly within $(-\frac{\pi}{4}, \frac{\pi}{4})$; (c) points sampled uniformly in a unit sphere.

Performance of our method in the noiseless setting. For the 1D setting we deduced in section 2 that the pairwise distance constraints by themselves are sufficient to identify the underlying 3D configuration. For the 2D setting we proved in section 3 that knowing additionally the distances between neighboring beads leads to uniqueness. We here perform simulations in 3D since this is the biologically relevant setting. These results are depicted in Figure 5 with additional examples in Figure SM1. The input to our algorithm are the pairwise distances (which are summed over homologs), all 3-way distances, the distances between homologous loci, and the distances between neighboring beads. In the noiseless setting considered here we solve the SDP formulation in Equation (5.1). Figure 5 and Figure SM1 show that the true and reconstructed structures highly overlap, thereby indicating that our optimization formulation is able to recover the 3D structure of the full diploid genome in the noiseless setting. When the 3-way distance constraints are removed, the reconstructions are less aligned with the true structures. This is shown in Figure 6, where we measure

the root-mean-square deviation (RMSD) between true and reconstructed 3D coordinates over 20 trials. In line with our theoretical results, these experimental results in the noiseless setting indicate the importance of higher-order contact frequencies for recovering the 3D diploid configuration, especially when the number of chromosomes is larger.

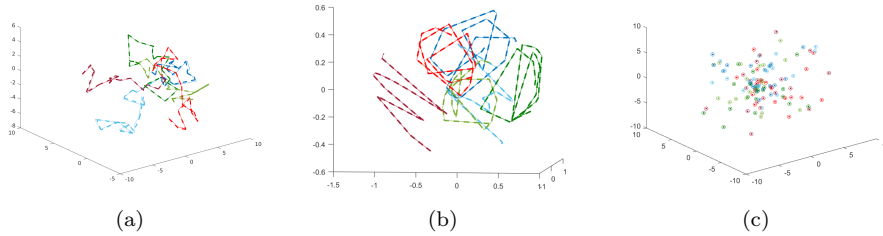


FIG. 5. Examples of true and reconstructed points on simulated data. (a) Brownian motion model. (b) Spirals. (c) Random points in a sphere. We generate six chromosomes with in total of 120 domains, corresponding to three homologous pairs with 20 domains per chromosome in the noiseless setting. Solid lines / points correspond to true 3D coordinates and dashed lines / unfilled points to reconstructions via our method. Each color represents a different chromosome.

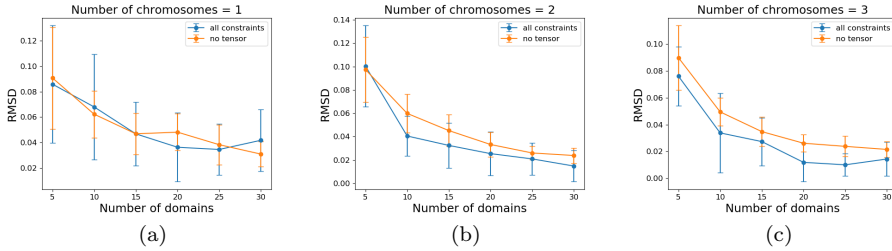


FIG. 6. Performance of our method in the noiseless setting. Root-mean-square deviation (RMSD) between true and reconstructed structure computed with and without higher-order distance constraints. Simulated data was generated using a Brownian motion model with (a) one (b) two and (c) three chromosomes. Mean and standard deviation over 20 trials are shown.

Performance of our method in the noisy setting. Next, we consider noisy distance observations $D_{ij} = D_{ij}^*(1 + \delta)$ and noisy 3-way distance observations $D_{i_1 i_2 \dots i_k} = D_{i_1 i_2 \dots i_k}^*(1 + \delta)$ by sampling δ uniformly within $(-\epsilon, \epsilon)$ as in [46], where ϵ is a given noise level. For our simulations we sample a maximum of 1000 3-way distance constraints. As shown in Figure SM2, we observe that the number of constraints does not have a major effect on the reconstruction accuracy. While for all simulations shown in this section, we set the tuning parameter $\rho = 0.000001$, Figure SM3 shows that the performance is not significantly different when using different choices of ρ .

In Figure 7 we numerically assess the accuracy of our predicted structure for the Brownian motion model for different number of chromosomes (one, two, or three) and different number of domains per chromosome (10 or 20) by computing the Spearman correlation between reconstructed and true pairwise distances, similar to [46]. As expected, Figure 7 shows that when the noise level increases, then the Spearman correlation between the original and reconstructed configuration decreases. For the

simulations with one chromosome, the Spearman correlation is higher for 20 domains than 10.

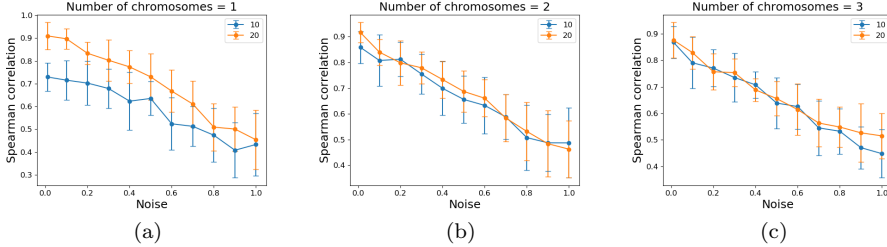


FIG. 7. Performance of our method in the noisy setting. Spearman correlation under different noise levels for (a) one, (b) two and (c) three chromosomes. Simulated data was generated using a Brownian motion model where each chromosome has 10 or 20 domains. Mean and standard deviation over 20 trials are shown.

6.2. Application to 3D diploid genome reconstruction. We apply our algorithm to the problem of reconstructing the diploid genome from contact frequency data derived from experiments. We obtain pairwise and 3-way contact frequencies collected via SPRITE in human lymphoblastoid cells from [33]. Since we aim to reconstruct the whole diploid genome, which consists of approximately 6 billion base pairs, for computational reasons we bin the contact frequencies in the SPRITE dataset into 10 Mega-base pair (Mb) regions. While some previous studies considered higher resolutions, the majority of the studies [4, 19, 36, 42, 46] did not attempt to reconstruct the whole diploid genome and focused only on reconstructing one chromosome, thus enabling them to consider higher resolutions.

After filtering out regions with a small number of total contacts, we obtain 514 unphased points on the chromosomes. We convert the pairwise contact frequencies to pairwise distances using the previously observed relationship $D_{ij} = F_{ij}^{-1/2}$ [36] and use Lemma 2.3 to obtain the distances between homolog pairs from this data. As in our simulations in the noisy setting, we randomly sample 1000 3-way distance constraints from all nonzero 3-way contact frequencies (for the transformation from 3-way contact frequencies to 3-way distances, see section 4). Finally, we obtain the distances between neighboring 10Mb beads by empirically evaluating the 3D reconstructions under different input distances; see section SM4 and Figure SM4, Figure SM5.

Using the pairwise constraints, homolog-homolog constraints, neighboring bead constraints, and 3-way distance constraints, we solve the SDP problem in Equation (5.2) for the noisy setting and analyze the corresponding 3D coordinates. Our diploid reconstruction is shown in Figure 8a. We compare this diploid genome reconstruction to the 3D structure obtained via ChromSDE, shown in Figure 8b obtained under the assumption that the observed contact frequencies and the corresponding distances are a sum of four equal quantities, i.e., $\|x_i - x_j\|^2$, $\|x_i - y_j\|^2$, $\|y_i - x_j\|^2$, and $\|y_i - y_j\|^2$ are equal. In Figure SM6, we show that the reconstruction obtained using ChromSDE with equal distances does not recapitulate known biology as described in the following paragraphs.

Experimental (imaging) studies have shown that chromosomes are organized by size within the nucleus, with small chromosomes in the interior and larger chromosomes on the periphery [3]. We colored each chromosome according to its size and

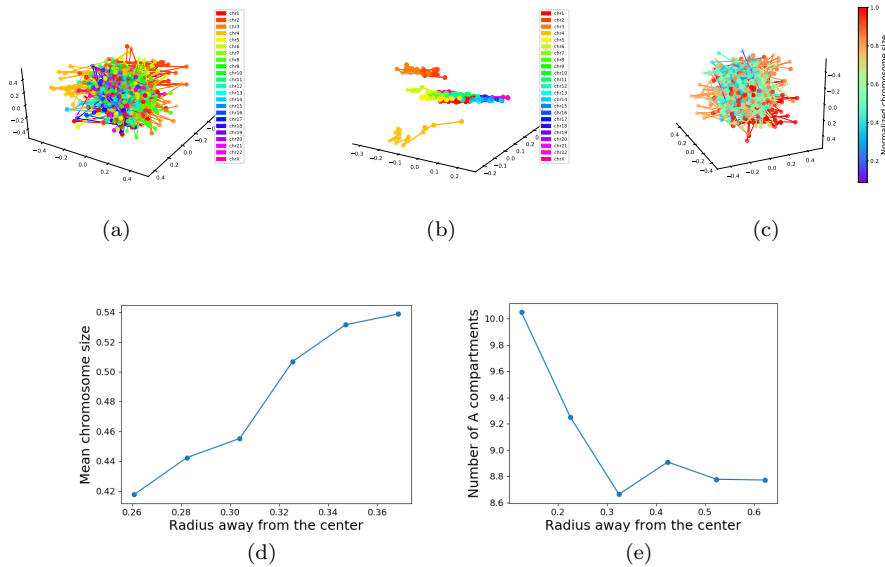


FIG. 8. *3D Diploid Genome Reconstruction. Estimated 3D positions of all chromosomes and their corresponding homologs at 10Mb resolution. 3D positions obtained using (a) our method and (b) using ChromSDE with chromosomes colored according to chromosome number. (c) Whole diploid organization obtained via our method, colored by chromosome size. (d) Mean chromosome size as the distance from the center increases. (e) The number of A compartments as the distance from the center increases.*

computed the mean chromosome size versus distance away from the center. The results of the 3D configuration obtained using our method are shown in [Figures 8c](#) and [8d](#) and recapitulate prior studies: smaller chromosomes are preferentially located in the center, whereas larger chromosomes are preferentially on the periphery; see also [section SM6](#), [Figure SM7](#). This is especially apparent for chromosomes 2 and 4, which are some of the largest chromosomes, and in our reconstruction they are located on the periphery as expected.

Experimental studies on the spatial organization of the genome have also shown that the center of the nucleus is enriched in active compartments (known as A compartments), while the periphery contains inactive compartments (known as B compartments) [38]. From previously published data on the location of A and B compartments along the genome in human lymphoblastoid cells [34], we counted the number of A compartments per 10Mb bin. Then dividing our 3D reconstruction into concentric circles of increasing radius away from the center, we found the mean number of A compartments in each concentric circle. [Figure 8e](#) shows that with increasing distance away from the center, the number of A compartments decreases. Thus, our reconstruction recovers the experimentally observed trend for A compartments to be preferentially located near the nucleus center. As shown in [Figures SM8](#) and [SM9](#) in [section SM7](#), we note that our results are robust to the choice of the tuning parameter ρ resulting in biologically plausible configurations independent of the choice of ρ .

Currently, many studies such as [35] simply ignore the fact that the genome is diploid and infer the 3D genome organization as if the data was collected from a haploid organism, assuming that the homologous loci have the same 3D structure.

However, we show in [section SM8](#), [Figure SM10](#) that the haploid distance matrices, computed by including only one copy of each of the homologous loci, are different between the two copies with a mean Spearman correlation of only 0.08. This shows that modeling the diploid aspect of the genome provides valuable information regarding the 3D structure of each of the homologs, which may be substantially different.

7. Discussion. In this paper, we proved that for a diploid organism the 3D genome structure is not identifiable from pairwise distance measurements alone. This implies that applying any algorithm for the reconstruction of the 3D genome structure from typical chromosome conformation capture data for a diploid organism can result in any of the infinitely many configurations with the same pairwise contact frequencies. We showed that unique identifiability is obtained using distance constraints between neighboring genomic loci as well as 3-way distance constraints in addition to the pairwise distance constraints that can be obtained from typical contact frequency data. Distances between neighboring genomic loci can be obtained empirically, e.g. from imaging studies, while 3-way distance constraints can be obtained from the most recently developed sequencing-based methods for obtaining contact frequencies such as SPRITE [33], C-walks [31] and GAM [2]. We also presented SDP formulations for determining the 3D genome reconstruction both in the noiseless and the noisy setting. Finally, we applied our algorithm to contact frequency data from human lymphoblastoid cells collected using SPRITE and showed that our results recapitulate known biological trends; in particular, in the 3D configuration identified using our method, the small chromosomes are preferentially situated in the interior of the cell nucleus, while the larger chromosomes are preferentially situated at the periphery of the cell nucleus. In addition, in the 3D configuration identified using our method the number of A domains is higher in the interior versus the periphery, which is in line with experimental results. Our work shows the importance of higher-order contact frequencies that can be measured using SPRITE [33], C-walks [31] and GAM [2] for obtaining the 3D organization of the genome in diploid organisms. This is particularly relevant for the reconstruction of cancer genomes, where copy number variations are frequent and hence the genome may contain even more than two copies of each locus.

We conjecture that identifiability of the 3D genome structure can also be achieved by replacing the higher-order contact constraints by distance constraints to the center of the cell nucleus. Such constraints are also biologically relevant, since these distances can be measured via imaging experiments, or inferred by measuring whether a particular locus is in a lamin-associated domain or a telomere, both of which tend to lie at the boundary of the cell nucleus [10, 18, 41]. Another future research direction is the development of specialized solvers to enable reconstruction of the genome at higher resolution. In this study we used a 10Mbp resolution due to the computational constraints imposed by SDP solvers. Finally, the theoretical results in this paper build on the assumption that distances are inverses of square roots of pairwise and higher-order contact frequencies. An interesting future research direction is to develop a method for estimating the map between higher-order contact frequencies and distances, and then prove identifiability as well as build reconstruction algorithms for these different maps.

Acknowledgements. We thank Mohab Safey El Din for helpful discussions.

- [1] A. Y. ALFAKIH, A. KHANDANI, AND H. WOLKOWICZ, *Solving Euclidean distance matrix completion problems via semidefinite programming*, Computational Optimization and Applications, 12 (1999), pp. 13–30.
- [2] R. A. BEAGRIE, A. SCIALDONE, M. SCHUELER, D. C. A. KRAEMER, M. CHOTALIA, S. Q. XIE, M. BARBIERI, I. DE SANTIAGO, L.-M. LAVITAS, M. R. BRANCO, ET AL., *Complex multi-enhancer contacts captured by genome architecture mapping*, Nature, 543 (2017), p. 519.
- [3] A. BOLZER, G. KRETH, I. SOLOVEI, D. KOEHLER, K. SARACOGLU, C. FAUTH, S. MÜLLER, R. EILS, C. CREMER, M. R. SPEICHER, ET AL., *Three-dimensional maps of all chromosomes in human male fibroblast nuclei and prometaphase rosettes*, PLoS Biology, 3 (2005), p. e157.
- [4] A. G. CAUER, G. YARDIMCI, J.-P. VERT, N. VAROQUAUX, AND W. S. NOBLE, *Inferring diploid 3D chromatin structures from Hi-C data*, bioRxiv:644294, (2019).
- [5] L. CAYTON AND S. DASGUPTA, *Robust Euclidean embedding*, in Proceedings of the 23rd International Conference on Machine Learning, ICML '06, New York, NY, USA, 2006, ACM, pp. 169–176.
- [6] V. CHANDRASEKARAN, B. RECHT, P. A. PARRILO, AND A. S. WILLSKY, *The convex geometry of linear inverse problems*, Foundations of Computational Mathematics, 12 (2012), pp. 805–849.
- [7] . G. P. CONSORTIUM ET AL., *An integrated map of genetic variation from 1,092 human genomes*, Nature, 491 (2012), pp. 56–65.
- [8] . G. P. CONSORTIUM ET AL., *A global reference for human genetic variation*, Nature, 526 (2015), pp. 68–74.
- [9] T. F. COX AND M. A. A. COX, *Multidimensional scaling*, Chapman and Hall / CRC, 2000.
- [10] L. CRABBE, A. J. CESARE, J. M. KASUBOSKI, J. A. J. FITZPATRICK, AND J. KARLSEDER, *Human telomeres are tethered to the nuclear envelope during postmitotic nuclear assembly*, Cell Reports, 2 (2012), pp. 1521–1529.
- [11] J. DEKKER, *Gene regulation in the third dimension*, Science, 319 (2008), pp. 1793–1794.
- [12] J. DEKKER, K. RIPPE, M. DEKKER, AND N. KLECKNER, *Capturing chromosome conformation*, Science, 295 (2002), pp. 1306–1311.
- [13] M. DI PIERRO, B. ZHANG, E. L. AIDEN, P. G. WOLYNES, AND J. N. ONUCHIC, *Transferable model for chromosome architecture*, Proceedings of the National Academy of Sciences, 113 (2016), pp. 12168–12173.
- [14] Z. DUAN, M. ANDRONESCU, K. SCHUTZ, S. MCILWAIN, Y. J. KIM, C. LEE, J. SHENDURE, S. FIELDS, C. A. BLAU, AND W. S. NOBLE, *A three-dimensional model of the yeast genome*, Nature, 465 (2010), pp. 363–367, <http://dx.doi.org/10.1038/nature08973>.
- [15] H. FANG AND D. P. O'LEARY, *Euclidean distance matrix completion problems*, Optimization Methods and Software, 27 (2012), pp. 695–717.
- [16] M. FAZEL, H. HINDI, AND S. P. BOYD, *Log-det heuristic for matrix rank minimization with applications to Hankel and Euclidean distance matrices*, in Proceedings of the 2003 American Control Conference, vol. 3, IEEE, 2003, pp. 2156–2162.
- [17] M. FAZEL, H. HINDI, S. P. BOYD, ET AL., *A rank minimization heuristic with application to minimum order system approximation*, in Proceedings of the American Control Conference, vol. 6, Citeseer, 2001, pp. 4734–4739.
- [18] L. GUELEN, L. PAGIE, E. BRASSET, W. MEULEMAN, M. B. FAZA, W. TALHOUT, B. H. EUSSEN, A. DE KLEIN, L. WESSELS, W. DE LAAT, ET AL., *Domain organization of human chromosomes revealed by mapping of nuclear lamina interactions*, Nature, 453 (2008), pp. 948–951.
- [19] M. HU, K. DENG, Z. QIN, J. DIXON, S. SELVARAJ, J. FANG, B. REN, AND J. S. LIU, *Bayesian inference of spatial organizations of chromosomes*, PLoS Computational Biology, 9 (2013), p. e1002893.
- [20] J. R. HUGHES, N. ROBERTS, S. MCGOWAN, D. HAY, E. GIANNOULATOU, M. LYNCH, M. DE GOBBI, S. TAYLOR, R. GIBBONS, AND D. R. HIGGS, *Analysis of hundreds of cis-regulatory landscapes at high resolution in a single, high-throughput experiment*, Nature Genetics, 46 (2014), pp. 205–212.
- [21] R. JUNGSMANN, M. S. AVENDAÑO, J. B. WOHRSTEIN, M. DAI, W. M. SHIH, AND P. YIN, *Multiplexed 3d cellular super-resolution imaging with dna-paint and exchange-paint*, Nature Methods, 11 (2014), p. 313.
- [22] N. KRISLOCK, *Semidefinite facial reduction for low-rank Euclidean distance matrix completion*, PhD thesis, University of Waterloo, 2010, <http://hdl.handle.net/10012/5093>.
- [23] A. LESNE, J. RIPOSO, P. ROGER, A. COUNAC, AND J. MOZZICONACCI, *3D genome reconstruction from chromosomal contacts*, Nature Methods, 11 (2014), pp. 1141–1143.
- [24] E. LIEBERMAN-AIDEN, N. L. V. BERKUM, L. WILLIAMS, M. IMAKAEV, T. RAGOCZY, A. TELLING, I. AMIT, B. R. LAJOIE, P. J. SABO, M. O. DORSCHNER, R. SANDSTROM, B. BERNSTEIN,

- M. A. BENDER, M. GROUDINE, A. GNIRKE, J. STAMATOYANNOPOULOS, L. A. MIRNY, E. S. LANDER, AND J. DEKKER, *Comprehensive mapping of long-range interactions reveals folding principles of the human genome*, *Science*, 326 (2009).
- [25] E. LIEBERMAN-AIDEN, N. L. VAN BERKUM, L. WILLIAMS, M. IMAKAEV, T. RAGOCZY, A. TELLING, I. AMIT, B. R. LAJOIE, P. J. SABO, M. O. DORSCHNER, R. SANDSTROM, B. BERNSTEIN, M. A. BENDER, M. GROUDINE, A. GNIRKE, J. STAMATOYANNOPOULOS, L. A. MIRNY, E. S. LANDER, AND J. DEKKER, *Comprehensive mapping of long-range interactions reveals folding principles of the human genome*, *science*, 326 (2009), pp. 289–293.
- [26] F. LU, S. KELES, S. J. WRIGHT, AND G. WAHBA, *Framework for kernel regularization with application to protein clustering*, *Proceedings of the National Academy of Sciences*, 102 (2005), pp. 12332–12337.
- [27] L. A. MIRNY, *The fractal globule as a model of chromatin architecture in the cell*, *Chromosome research*, 19 (2011), pp. 37–51.
- [28] B. MISHRA, G. MEYER, AND R. SEPULCHRE, *Low-rank optimization for distance matrix completion*, in 2011 50th IEEE Conference on Decision and Control and European Control Conference, 2011, pp. 4455–4460.
- [29] I. MÜLLER, S. BOYLE, R. H. SINGER, W. A. BICKMORE, AND J. R. CHUBB, *Stable morphology, but dynamic internal reorganisation, of interphase human chromosomes in living cells*, *PLoS One*, 5 (2010), p. e11560.
- [30] G. NIR, I. FARABELLA, C. P. ESTRADA, C. G. EBELING, B. J. BELIVEAU, H. M. SASAKI, S. H. LEE, S. C. NGUYEN, R. B. MCCOLE, S. CHATTORAJ, ET AL., *Walking along chromosomes with super-resolution imaging, contact maps, and integrative modeling*, *PLoS Genetics*, 14 (2018), p. e1007872.
- [31] P. OLIVARES-CHAUVET, Z. MUKAMEL, A. LIFSHITZ, O. SCHWARTZMAN, N. O. ELKAYAM, Y. LUBLING, G. DEIKUS, R. P. SEBRA, AND A. TANAY, *Capturing pairwise and multi-way chromosomal conformations using chromosomal walks*, *Nature*, 540 (2016), pp. 296–300.
- [32] Y. QI AND B. ZHANG, *Predicting three-dimensional genome organization with chromatin states*, *PLoS computational biology*, 15 (2019), p. e1007024.
- [33] S. A. QUINODOZ, N. OLLIKAINEN, B. TABAK, A. PALLA, J. M. SCHMIDT, E. DETMAR, M. M. LAI, A. A. SHISHKIN, P. BHAT, Y. TAKEI, ET AL., *Higher-order inter-chromosomal hubs shape 3D genome organization in the nucleus*, *Cell*, 174 (2018), pp. 744–757.
- [34] S. S. P. RAO, M. H. HUNTLEY, N. C. DURAND, E. K. STAMENOVA, I. D. BOCHKOV, J. T. ROBINSON, A. L. SANBORN, I. MACHOL, A. D. OMER, E. S. LANDER, ET AL., *A 3D map of the human genome at kilobase resolution reveals principles of chromatin looping*, *Cell*, 159 (2014), pp. 1665–1680.
- [35] L. RIEBER AND S. MAHONY, *miniMDS: 3D structural inference from high-resolution Hi-C data*, *Bioinformatics*, 33 (2017), pp. i261–i266.
- [36] M. ROUSSEAU, J. FRASER, M. A. FERRAIUOLO, J. DOSTIE, AND M. BLANCHETTE, *Three-dimensional modeling of chromatin structure from interaction frequency data using Markov chain Monte Carlo sampling*, *BMC Bioinformatics*, 12 (2011), p. 414.
- [37] M. SIMONIS, P. KLOUS, E. SPLINTER, Y. MOSHKIN, R. WILLEMSEN, E. DE WIT, B. VAN STEENSEL, AND W. DE LAAT, *Nuclear organization of active and inactive chromatin domains uncovered by chromosome conformation capture-on-chip (4C)*, *Nature Genetics*, 38 (2006), pp. 1348–1354.
- [38] T. J. STEVENS, D. LANDO, S. BASU, L. P. ATKINSON, Y. CAO, S. F. LEE, M. LEEB, K. J. WOHLFAHRT, W. BOUCHER, A. O’SHAUGHNESSY-KIRWAN, ET AL., *3D structures of individual mammalian genomes studied by single-cell Hi-C*, *Nature*, 544 (2017), p. 59.
- [39] C. UHLER AND G. V. SHIVASHANKAR, *Chromosome intermingling: mechanical hotspots for genome regulation*, *Trends in Cell Biology*, 27 (2017), pp. 810–819.
- [40] C. UHLER AND G. V. SHIVASHANKAR, *The regulation of genome organization and gene expression by nuclear mechanotransduction*, *Nature Reviews Molecular Cell Biology*, 18 (2017), pp. 717–727.
- [41] B. VAN STEENSEL AND A. S. BELMONT, *Lamina-associated domains: links with chromosome architecture, heterochromatin, and gene repression*, *Cell*, 169 (2017), pp. 780–791.
- [42] N. VAROQUAUX, F. AY, W. S. NOBLE, AND J.-P. VERT, *A statistical approach for inferring the 3D structure of the genome*, *Bioinformatics*, 30 (2014), pp. i26–i33.
- [43] H. WANG, X. XU, C. M. NGUYEN, Y. LIU, Y. GAO, X. LIN, T. DALEY, N. H. KIPNISS, M. LA RUSSA, AND L. S. QI, *CRISPR-mediated programmable 3D genome positioning and nuclear organization*, *Cell*, 175 (2018), pp. 1405–1417.
- [44] K. Q. WEINBERGER, F. SHA, Q. ZHU, AND L. K. SAUL, *Graph Laplacian regularization for large-scale semidefinite programming*, in *Advances in Neural Information Processing Systems*, 2007, pp. 1489–1496.

- [45] L. ZHANG, G. WAHBA, AND M. YUAN, *Distance shrinkage and Euclidean embedding via regularized kernel estimation*, Journal of the Royal Statistical Society: Series B, 78 (2016), pp. 849–867.
- [46] Z. ZHANG, G. LI, K.-C. TOH, AND W.-K. SUNG, *3D Chromosome Modeling with Semi-Definite Programming and Hi-C Data*, Journal of Computational Biology, 20 (2013).

SUPPLEMENTARY MATERIALS: IDENTIFYING 3D GENOME ORGANIZATION IN DIPLOID ORGANISMS VIA EUCLIDEAN DISTANCE GEOMETRY*

ANASTASIYA BELYAEVA[†], KAIE KUBJAS[‡], LAWRENCE J. SUN[†], AND CAROLINE UHLER[†]

SM1. Simulations: reconstructions in the noiseless setting. Figure SM1 shows additional reconstructions of simulated data in the noiseless setting. The true structures are consistently recovered under different data generation models.

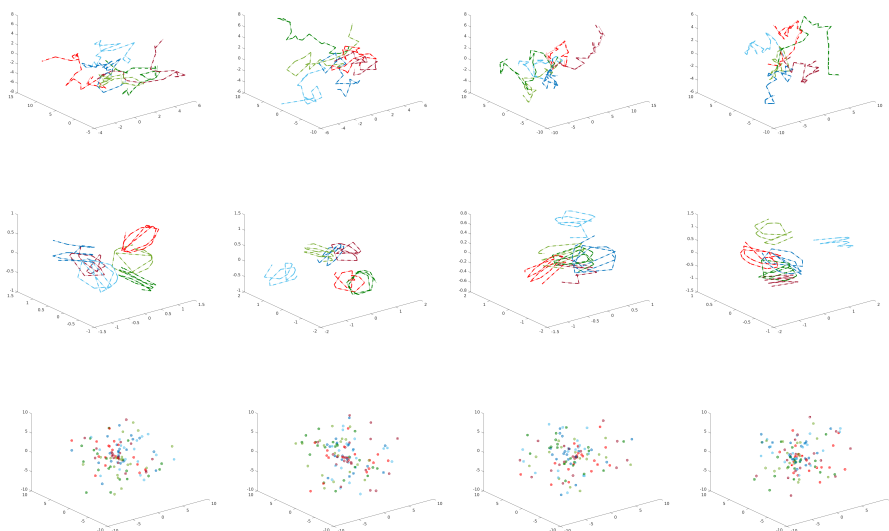


FIG. SM1. Additional examples of true and reconstructed points on simulated data. True points were generated using Brownian motion model (first row), spirals (second row) and random points in a sphere (third row). We generated six chromosomes, corresponding to three homologous pairs with 20 domains per chromosome in the noiseless setting. Solid lines / points correspond to true 3D coordinates and dashed lines / unfilled points to reconstructions via our method. Each color represents a different chromosome.

*Submitted.

Funding: Anastasiya Belyaeva was supported by an NSF Graduate Research Fellowship (1122374), the Abdul Latif Jameel World Water and Food Security Lab (J-WAFS) at MIT and the MIT J-Clinic for Machine Learning and Health. Kaie Kubjas was supported by the European Union’s Horizon 2020 research and innovation programme: Marie Skłodowska-Curie grant agreement No. 748354, research carried out at LIDS, MIT and Team PolSys, LIP6, Sorbonne University. Caroline Uhler was partially supported by NSF (DMS-1651995), ONR (N00014-17-1-2147 and N00014-18-1-2765), IBM, and a Simons Investigator Award.

[†]Laboratory for Information and Decision Systems, Department of Electrical Engineering and Computer Science, and Institute for Data, Systems and Society, Massachusetts Institute of Technology, Cambridge, MA (belyaeva@mit.edu, sunl@mit.edu, cuhler@mit.edu).

[‡]Department of Mathematics and Systems Analysis, Aalto University, Espoo, Finland (kaie.kubjas@aalto.fi).

SM2. Simulations: impact of the number of 3-way distance constraints.

Figure SM2 shows the impact of the number of 3-way distance constraints on the solution in the noisy setting. We explored the impact of the number of 3-way distance constraints specifically when the number of chromosomes is higher (three chromosomes) since higher-order constraints seem to play a more critical role in that setting. We evaluate the performance when 500, 1000 or all (4060 for 30 domains) 3-way distance constraints are used. Figure SM2 shows that the choice of the number of 3-way distance constraints has little impact on the accuracy of reconstruction, so we used 1000 3-way distance constraints (or all possible triplets if that number was smaller) for the simulations and the real data analysis.

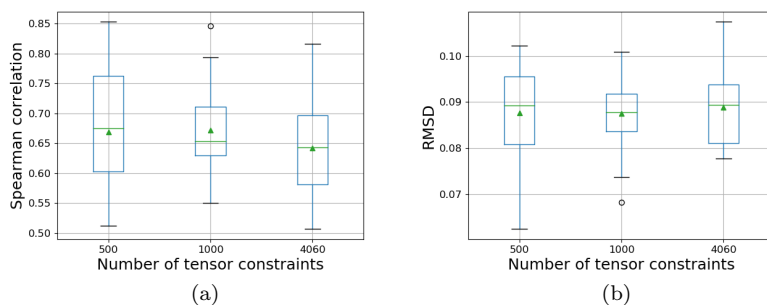


FIG. SM2. *The impact of the number of 3-way distance constraints in the noisy setting. Boxplots showing Spearman correlation and root-mean-square deviation (RMSD) for different number of 3-way distance constraints over 20 trials. Simulated data was generated using Brownian motion model with three chromosomes, where each chromosome had 10 domains. Noise level of 0.5 was added. We used $\rho = 0.000001$ to solve the SDP. Green triangles and lines indicate the mean and median performance respectively.*

SM3. Simulations: impact of the tuning parameter ρ . Figure SM3 explores the impact of the tuning parameter ρ in the noisy setting. Figure SM3 shows that the choice of ρ has little impact on the accuracy of the reconstruction. For the simulations in the noisy setting and for real data we chose $\rho = 0.000001$.

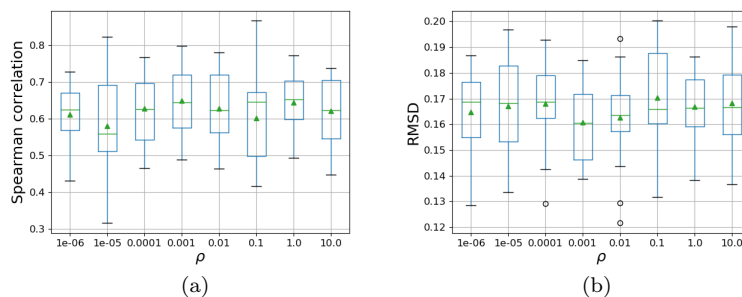


FIG. SM3. *The impact of ρ in the noisy setting. Boxplots showing Spearman correlation and root-mean-square deviation (RMSD) for different values of ρ over 20 trials. Simulated data was generated using a Brownian motion model with one chromosome and 10 domains per chromosome as well as noise level of 0.5. We used the maximum number of triplet tensor constraints (120) to solve the SDP. Green triangles and lines indicate the mean and median performance respectively.*

SM4. Distance between neighboring beads. We consider different values for the distance between neighboring beads as input to our algorithm. If the distance between neighboring beads is chosen to be too small, the resulting 3D diploid reconstruction of the data results in the homologous loci x_1, \dots, x_n (copy A) and y_1, \dots, y_n (copy B) being completely separated as shown in Figure SM4a. We gradually increased the values for the distance between neighboring beads and quantified the separation between x_1, \dots, x_n and y_1, \dots, y_n as follows: We obtained the hyperplane separating x_1, \dots, x_n and y_1, \dots, y_n by fitting a support-vector machine (SVM) classifier. Next, we identified the k points among x_1, \dots, x_n as well as among y_1, \dots, y_n that are closest to the hyperplane and computed their centroids. Figure SM4b shows the sum of the distances of the two centroids to the separating hyperplane, thereby quantifying the separation of the copy A points from the copy B points. This distance should approach 0 as the copy A and copy B points come closer together. Indeed, Figure SM4b shows that using a parameter of 0.65, the distance between the k closest points stabilizes close to 0 and thus we used 0.65 as the distance between neighboring beads.

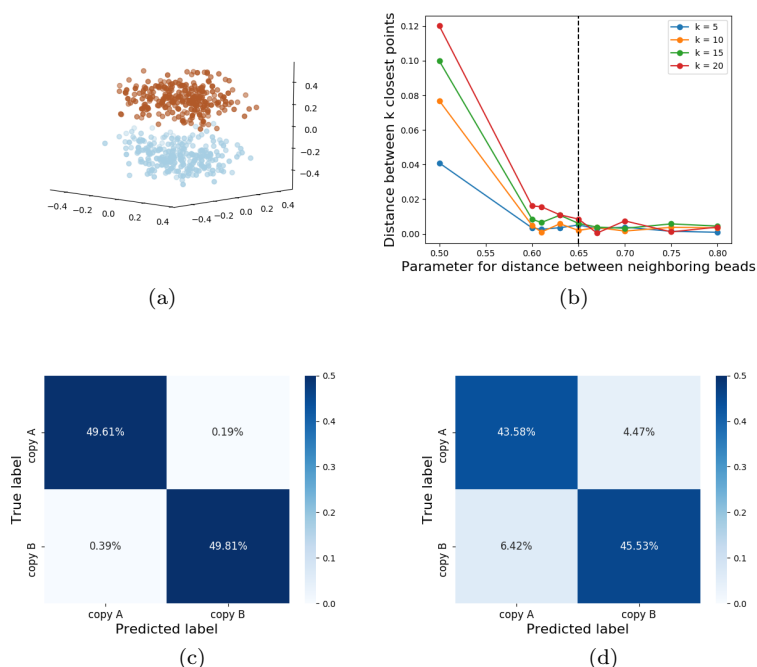


FIG. SM4. Empirical choice of parameter for the distance between neighboring beads. (a) The 3D genome reconstruction with parameter for the distance between neighboring beads set to 0.5. The homologous loci x_1, \dots, x_n (copy A) and y_1, \dots, y_n (copy B), colored by red and blue are completely separated. (b) The distance of centroids corresponding to k closest points to the SVM hyperplane separating copy A from copy B (red and blue points) for different parameter settings. The black dashed line corresponds to the chosen parameter of 0.65. (c) Confusion matrix quantifying how often points clustered via k -means (predicted label) were assigned their true label (copy A or copy B) when parameter of 0.5 was used. (d) Same as (c) for the chosen parameter 0.65. Higher confusion across labels indicates that points belonging to copy A and copy B are not clearly separated, as desired.

We provide additional quantification regarding the separation of points in copy

A and copy B by clustering the 3D structure using k -means into two clusters and computing a confusion matrix, where the true labels are given by copy A and copy B. If the points x_1, \dots, x_n and y_1, \dots, y_n are completely separated, then k -means would result in near perfect accuracy of separation of all points into copy A and copy B. Figure SM4c shows that this is indeed the case when using a distance parameter of 0.5. For the chosen parameter of 0.65, the confusion matrix is shown in Figure SM4d, reinforcing the observation that indeed copy A and copy B are getting mixed.

We note that our observations are robust to the exact choice of the distance between neighboring beads. In Figure SM5 we show the resulting 3D reconstruction as well as chromosome size and A compartment trends when using a parameter of 0.7 as the distance between neighboring beads.

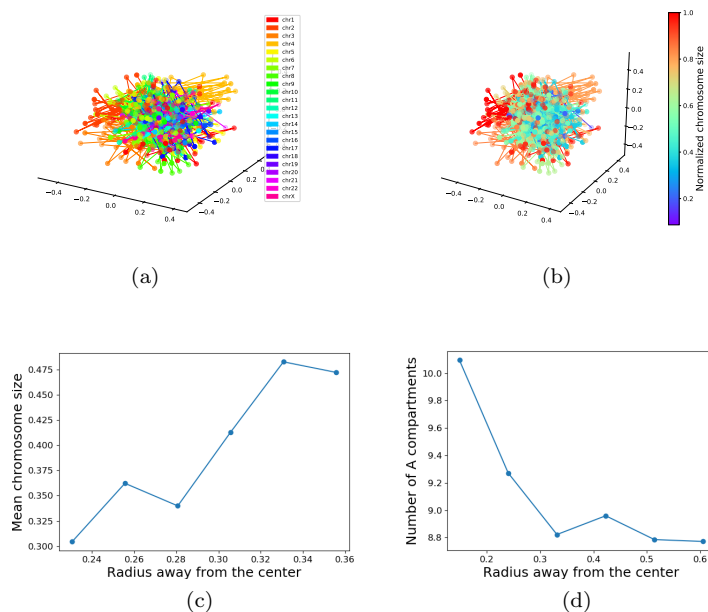


FIG. SM5. 3D diploid genome reconstruction with a different parameter (0.7 instead of 0.65) for the distance between neighboring beads. (a) Estimated 3D positions of all chromosomes and their corresponding homologs with chromosomes colored according to chromosome number. (b) Whole diploid organization obtained via our method, colored by chromosome size. (c) Mean chromosome size as the distance from the center increases. (d) The number of A compartments as the distance from the center increases.

SM5. Comparison with ChromSDE. We compare our whole genome reconstruction to the reconstruction inferred by ChromSDE [SM3]. Since ChromSDE does not account for the fact that the measured contact frequencies and corresponding observed distances are a sum of four different distances, i.e. $\|x_i - x_j\|^2$, $\|x_i - y_j\|^2$, $\|y_i - x_j\|^2$, and $\|y_i - y_j\|^2$, we converted frequencies to distances using $D_{ij} = F_{ij}^{-1/2}$ and used $D_{ij}/4$ for each of the four distances so that the diploid configuration of the genome could be computed. We assumed that homologous loci are far apart, as has been observed in imaging studies [SM1, SM2], and thus set $\|x_i - y_i\|^2 = \infty$. Given the described distance constraints, we solved the SDP for the Gram matrix and ob-

tained the 3D coordinates using eigenvector decomposition, similar to our method. Figure SM6 shows the corresponding solution and quantification of the mean chromosome size and number of A compartments as the radius from the center increases. The computed 3D diploid genome configuration obtained via ChromSDE does not recapitulate that chromosome size increases with distance away from the center and that the number of A compartments decreases with distance away from the center.

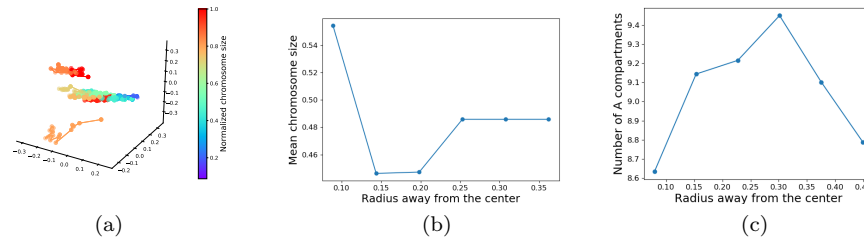


FIG. SM6. 3D diploid genome reconstruction with ChromSDE. ChromSDE was run using a distance matrix where the distances for $\|x_i - x_j\|^2$, $\|x_i - y_j\|^2$, $\|y_i - x_j\|^2$, and $\|y_i - y_j\|^2$ were set to $D_{i,j}/4$. (a) Estimated 3D positions of all chromosomes and their corresponding homologs at 10Mb resolution colored by chromosome size. (b) Mean chromosome size as the distance from the center increases. (c) The number of A compartments as the distance from the center increases.

SM6. Analysis of 3D diploid genome reconstruction. We provide further analysis of the 3D diploid genome reconstruction obtained using our algorithm from contact frequency data. Figure SM7 shows that chromosome size is correlated with the distance of the chromosome to the center of the cell nucleus, which is in line with known biological trends.

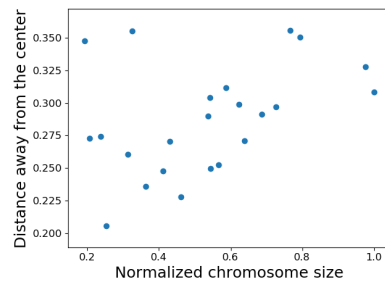


FIG. SM7. Chromosome size (normalized by the size of the largest chromosome) versus the mean distance of the chromosome and its homolog away from the center.

SM7. Real data: impact of the tuning parameter ρ . Figure SM8 explores the impact of the tuning parameter ρ on the results of the real data analysis. We compute the RMSD between the 3D genome reconstruction computed with $\rho = 0.000001$ and the 3D genome reconstructions computed with other choices of $\rho \in (0.00001, 0.0001, 0.001, 0.01, 0.1, 10, 1)$ to quantify how much the 3D structure changes when increasing ρ . As shown in Figure SM8, the RMSD is low across different choices of the tuning parameter. In Figure SM9, we provide the 3D genome

reconstruction and trends for mean number of A compartments and mean chromosome size versus the distance away from the center for the 3D reconstruction computed with $\rho = 10$ since the RMSD was the highest for this choice of the tuning parameter. We observe that the trends remain the same also for this choice of ρ .

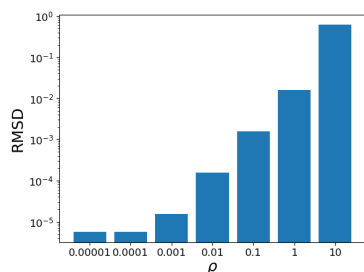


FIG. SM8. *The impact of ρ in real data. Root-mean-square deviation (RMSD) between the 3D genome reconstruction computed with $\rho = 0.000001$ and the 3D genome reconstructions computed with other choices of $\rho \in (0.00001, 0.0001, 0.001, 0.01, 0.1, 1, 10)$.*

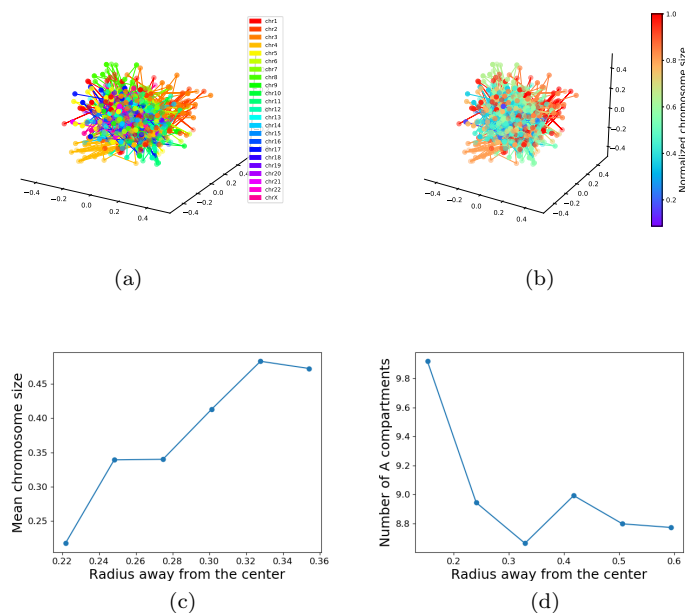


FIG. SM9. *3D diploid genome reconstruction with $\rho = 10$. Estimated 3D positions of all chromosomes and their corresponding homologs at 10Mb resolution. Chromosomes are colored according to (a) chromosome number and (b) chromosome size. (c) Mean chromosome size as the distance from the center increases. (d) The number of A compartments as the distance from the center increases.*

SM8. Haploid distance matrices. To show that modeling the diploid aspect of the genome is critical and provides valuable information regarding the 3D organization of the genome, we randomly labeled each homolog of a particular chromosome to correspond to either copy A or copy B of the chromosome and computed the Euclidean

distances between all loci belonging to copy A, i.e. $\|x_i - x_j\|$ to obtain one haploid distance matrix and the Euclidean distances between all loci belonging to copy B, i.e. $\|y_i - y_j\|$ to obtain the second haploid distance matrix. Figure SM10a and Figure SM10b show the haploid distance matrices where the points $1, \dots, n$ are assigned to copy A and points $n + 1, \dots, 2n$ are assigned to copy B. We were interested in comparing the two haploid distance matrices to see whether the two haploid matrices were the same or if modeling the diploid aspect of the genome also allowed us to learn about each homolog. Inspection of the two matrices reveals that the distances are different in these two haploid matrices, suggesting that modeling the genome as a diploid structure is important and indeed provides additional information. We quantify the difference by computing the Spearman correlation between the distance matrices over 100 different samplings of assignments of chromosomes to either copy A or B. Figure SM10c shows the histogram of the calculated Spearman correlations with mean Spearman correlation of 0.08.

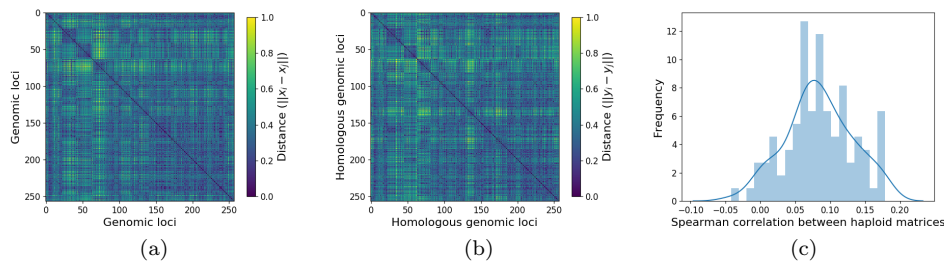


FIG. SM10. *Haploid distance matrices. (a) Haploid distance matrix for points belonging to copy A and (b) its corresponding homologous haploid distance matrix for points belonging to copy B. (c) Spearman correlation between haploid distance matrices over 100 different assignments of each homolog to either copy A or copy B.*

REFERENCES

- [SM1] A. BOLZER, G. KRETH, I. SOLOVEI, D. KOEHLER, K. SARACOGLU, C. FAUTH, S. MÜLLER, R. EILS, C. CREMER, M. R. SPEICHER, ET AL., *Three-dimensional maps of all chromosomes in human male fibroblast nuclei and prometaphase rosettes*, PLoS Biology, 3 (2005), p. e157.
- [SM2] G. NIR, I. FARABELLA, C. P. ESTRADA, C. G. EBELING, B. J. BELIVEAU, H. M. SASAKI, S. H. LEE, S. C. NGUYEN, R. B. MCCOLE, S. CHATTORAJ, ET AL., *Walking along chromosomes with super-resolution imaging, contact maps, and integrative modeling*, PLoS Genetics, 14 (2018), p. e1007872.
- [SM3] Z. ZHANG, G. LI, K.-C. TOH, AND W.-K. SUNG, *3D Chromosome Modeling with Semi-Definite Programming and Hi-C Data*, Journal of Computational Biology, 20 (2013).